DYNAMIC MODELING AND VIBRATION CONTROL OF A SINGLE-LINK FLEXIBLE MANIPULATOR USING A COMBINED LINEAR AND ANGULAR VELOCITY FEEDBACK CONTROLLER

by

Kerem Gurses
B.Eng., Istanbul Technical University, 2005

A Thesis Submitted in Partial Fulfillment of the
Requirements for the Degree of

MASTER OF APPLIED SCIENCE

in the Department of Mechanical Engineering

DYNAMIC MODELING AND VIBRATION CONTROL OF A SINGLE-LINK FLEXIBLE MANIPULATOR USING A COMBINED LINEAR AND ANGULAR VELOCITY FEEDBACK CONTROLLERS

by

Kerem Gurses

B.Eng., Istanbul Technical University, 2005

Supervisory Committee

Dr. Edward J. Park (Department of Mechanical Engineering)

Supervisor

Dr. Bradley J. Buckham (Department of Mechanical Engineering)

Supervisor

Dr. Afzal Suleman (Department of Mechanical Engineering)

Departmental Member

Dr. Panajotis Agathoklis (Department of Electrical and Computer Engineering)

External Examiner

ABSTRACT

The use of lightweight, thin flexible structures creates a dilemma in the aerospace and robotic industries. While increased operating efficiency and mobility can be achieved by employing such structures, these benefits are compromised by significant structural vibrations due to the increased flexibility. To address this problem, extensive research in the area of vibration control of flexible structures has been performed over the last two decades. The majority of the research has been based on the use of discrete piezoceramic actuators (PZTs) as active dampers, as they are commercial availability and have high force and bandwidth capabilities. Many different active vibration control strategies have previously been proposed, in order to effectively suppress vibrations. The synthesized vibration controllers will be less effective or even make the system to become unstable if the actuator locations and control gains are not chosen properly. However, there is currently no quantitative procedure that deals with these procedures simultaneously.

This thesis presents a theoretical and numerical study of vibration control of a single-link flexible manipulator attached to a rotating hub, with PZTs bonded to the surface of the link. A commercially available fibre optic sensor called ShapeTape^{TM} is introduced as a new feedback sensing technique, which is complemented by a quantitative and definitive model based procedure for selecting the individual PZT locations and gains. Based on Euler-Bernoulli beam theory, discrete finite element equations are obtained using Lagrange's equations for a PZT-mounted beam element. Slewing of the flexible link by a rotating hub induces vibrations in the link that persist long after the hub stops rotating. These vibrations are suppressed through a combined scheme of PD-based hub motion control and proposed PZT actuator control, which is a composite linear (L-type)

and angular (A-type) velocity feedback controller. A Lyapunov approach was used to synthesize the PZT controller. The feedback sensing of linear and angular velocities is realized by using the ShapeTape^{TM}, which measures the bend and twist of the flexible link's centerline. Both simulation and experimental results show that tip vibrations are most effectively suppressed using the proposed composite controller. Its performance advantage over the individual linear or angular velocity feedback controllers confirms theoretical predictions made based on a non-proportional damping model of the PZT effects. Furthermore, it is demonstrated that the non-proportional nature of the PZT damping effect must be considered in order to bound the range of allowable controller gain values.

Examiners

Dr. Edward J. Park (Department of Mechanical Engineering)

Supervisor

Dr. Bradley J. Buckham (Department of Mechanical Engineering)

Supervisor

Dr. Afzal Suleman (Department of Mechanical Engineering)

Departmental Member

Dr. Panajotis Agathoklis (Department of Electrical and Computer Engineering)

External Examiner

TABLE OF CONTENTS

LIST OF FIGURES

LIST OF TABLES

NOMENCLATURE

A	cross sectional area
a_k	growth or attenuation of the response
b_k	Cyclic frequency of the oscillations
C	PZT bending moment coefficient
$\mathbf{C}$	damping matrix
$\mathbf{d}$	Displacement vector
d_{iy}	nodal transverse displacement
d_{31}	dielectric constant of the PZT
$\mathbf{F}$	force vector
I	beam cross sectional moment of inertia
$\mathbf{I}$	Identity matrix
k_A	control gain for A-Type control strategy
k_L	control gain for L-Type control strategy
k_p	proportional gain on hub controller
k_v	Velocity gain on hub controller
k_i	beam element stiffness
$\mathbf{K}$	stiffness matrix
L	beam element length
M	Bending moment
m_i	elemental bending moment
m_i	beam element mass
$\mathbf{M}$	mass matrix
$\mathbf{N}$	shape functions vector
$\boldsymbol{r}$	Position vector
S	unstretched arc length
T	Time
$\hat{\boldsymbol{t}}$ 、 $\hat{\boldsymbol{n}}$ 、 $\hat{\boldsymbol{b}}$	Frenet reference frame
T	kinetic energy
$u(t)$	input torque to the hub

U	elastic strain energy
V	Lyapunov function candidate
V	potential energy
w	transverse displacement
δW	virtual work
$\hat{x}, \hat{y}\ \hat{z},$	elemental reference frame
x, y, z	local reference frame
X, Y, Z	global reference frame
α	substructure equilibrium parameter
ε	axial strain
γ	strain in the PZT bonding layer
κ	Curvature
ϕ_i	nodal rotational displacement
ρ	density
θ	hub angle
ψ	effective stiffness ratio
Λ	piezoelectric strain
Γ	non-dimensional shear transfer parameter
σ	Stress
τ	Applied shear stress/geometric torsion
ψ, θ, ϕ	yaw pitch and roll angles of the frenet frame
$\dot{(\ )}$	differentiation of $(\ )$ with respects to time
$(\ )'$	differentiation of $(\ )$ with respects to displacement
$(\ )_G$	global matrix of $(\ )$

ACKNOWLEDGEMENT

I would like to take this opportunity to express my appreciation to those who helped me complete this thesis.

First of all, I owe many thanks to my supervisors, Dr. Bradley J. Buckham and Dr. Edward J. Park for their guidance, advice and encouragement. Their constant support made this work possible. I have learned a lot from them; not only scientific knowledge, but also professionalism.

I would like to thank all my professors, colleagues and friends in the Department of Mechanical Engineering at the University of Victoria for the encouragement and friendship during the period of my study.

Special thanks to my parents, and my brother for their constant support during my entire life.

DEDICATION

To my parents and my brother.

Chapter 1 INTRODUCTION

1.1 Motivation

In the past two decades, the study of flexible link manipulators has been an active research area [1-7]. Such robots are lightweight and the reduction in mass affords high speed and energy efficient operations in aerospace applications. However, more pronounced vibrations are experienced due to the higher flexibility and the tendency for the link natural frequencies to drop nearer the frequency of actuation. The vibrations in flexible link manipulators can compromise the accuracy of their end-effector, produce instabilities and ultimately lead to structural failure due to fatigue. To minimize vibration and mitigate these dangers, a solution is the employment of an active control strategy, coupled with sensors and actuators, in order to enhance the stiffness and damping properties of the flexible link.

A flexible structure, such as the flexible link, that utilizes embedded smart materials is often referred to as a smart structure. Typically, piezoelectric actuators are used as smart

actuators, which are embedded in or bonded to the structure, to enhance the stiffness of the flexible link. Through the proper choice of mounting locations, the method by which the piezoelectric actuators are embedded, and the manner in which control voltages are applied, the piezoelectric actuators can be used to effectively attenuate elastic deformation (i.e. vibration) of the flexible link.

1.2 Theoretical Background

Of possible smart materials as actuators, piezoelectric materials are seeing the broadest application in flexible link manipulation given the inherent synergy between them and lightweight applications [18]: the actuators themselves are lightweight and leave a minimal mechanical footprint on the system they complement. They display excellent linearity over their dynamic range making them easy to model and hence control automatically. In addition, there are no moving parts and are reliable components in autonomous or remote applications.

Generally two types of piezoelectric composites are used:

(i) Lead zirconate titanate, hereafter referred as PZT.

(ii) Polyvinylidene fluoride, hereafter referred as PVDF.

A PZT or PVDF bonded to, or embedded within, a beam can create a shearing strain distribution over the beam surface(s), the net effect of which is an internal bending moment. Properly scheduled, the internal moment(s) damp the externally excited vibrations. An advantage of PZT over PVDF actuators is that PZTs generate significantly larger shearing force with the same applied voltage. However, due to logistic constraints

in the manufacturing process, the PZTs are produced as small patches while the PVDF actuators can be manufactured as one uniform layer [1,18]. The choice of PZT over PVDF includes the trade off of having a larger damping ability but also being subject to a complicated control problem since each segment of PZT should be controlled separately.

Studies on active vibration control of flexible links using multiple PZTs have relied extensively on modeling these links with flexible beams. The assumed modes method or the finite element method is most often used to obtain the discretized finite-dimensional dynamic model for the flexible link [1,5-6]. Two cases have been discussed in literature: a beam attached to a rotating hub or a stationary clamped free beam. The rotating beam case includes a coupling of an induced elastic deformation and a rigid-body slewing of the flexible beam about the hub axis. The lack of any significant structural damping causes the vibrations to persist long after the hub stops rotating. Yigit et al. [11] derived equations of motion for the rotating flexible beams and demonstrated that the rigid body mode contributes a centrifugal stiffening effect. Crawley et al. [12] presented the static and dynamic responses of a rotating beam equipped with both embedded and surface bonded PZT actuators. They also showed that the shear stress developed between the beam and piezoelectric surfaces is transferred over small zones close to the end of the PZT material. In the case of a perfectly bonded actuator, one where the boding layer has an infinitesimal thickness, Crawley demonstrated that the net effect of the PZT is a opposing pair of bending moments located at the ends of the actuated region – a model used by many researchers [1-5, 7].

The closed-loop control of the surface-mounted or embedded PZT actuators has been accomplished using different control techniques, including L-Type (linear velocity

feedback) control [1], strain rate feedback control [5], the LQG/LTR approach [4], Type II fuzzy logic [2], model reference control algorithms [6] and Kalman filtering approach [7]. Within any of these methodologies, a critical sub-problem is ensuring the stability of the actuated beam. Sun et al. [1] noted that the stability of an L-type PZT controller could be compromised if the actuators were located away from inflection points – points with zero surface strains. In [1], a Lyapunov candidate function is used to bound the gains on the feedback terms, but that analysis does not guarantee stability nor optimize the gain values within the suggested domain of stable values. The main premise in [1] is to suppress the lower modes of vibration by stiffening the system, raising the natural frequency of vibration, and limiting the amplitude of the response to a lower frequency disturbance. In addition to the stiffening effect of surface bonded PZTs, centrifugal stiffening caused by the hub rotation is used in that work. Due to the fact that the centrifugal stiffening is significant in the overall beam response, it is not clear what role the L-type control plays in the results of [1].

An alternative to the L-type, the A-type (angular velocity feedback) controller, has seen limited application. This is due to an inability to generate feedback of the angular velocity at the sensing points using conventional sensors (i.e. accelerometers and MEMS gyros). A contribution of the work presented in this thesis is the introduction of ShapeTape^{TM}, a sensor readily capable of measuring the angular displacements, and hence relative angular velocity, at discrete points along a flexible beam.

Another problem addressed in this work is the placement of the PZT actuators to obtain the optimum vibration suppression. Many researchers have sought for an answer to this problem by using different optimization techniques and performance measures.

For example, Zhang et al. [13] proposed to maximize the controllability and the observability of the controlled modes and minimize these same properties of residual modes. Fahroo et al. [14] and Hiramoto et al. [15] considered different performance measures that were based on their LQR controller's cost functions. Maxwell et al. [16] considered a simulated annealing technique to obtain the best actuator placement. The simulated annealing based optimization method was designed to allow placement of any number of discrete actuators of unequal length. A linear-quadratic-regulator controller function was used as part of the optimization procedure in [16] as well.

1.3 Research Objectives and Contributions

The main objectives of this thesis are: (i) to present a linear finite element model of a single-link flexible manipulator with surface bonded piezoceramics that undergoes a slewing maneuver by a rotating hub; (ii) to use a novel fiber optic sensor array, called ShapeTape^{TM}, as an embedded feedback sensor for sensing both linear and angular deformations of the flexible manipulator; (iii) to execute the simulation based design and the experimental evaluation of three types of vibration controllers, namely A-type, L-type and composite (A-type + L-type) controllers, and; (iv) to provide a procedure, based on a fundamental generalized eigenvalue problem, for determining the optimal locations and gains for the individual PZT actuators.

A fair and thorough comparison of the A-type and L-type controllers is missing from the current literature, and this research aims to fill this need. Additionally, this work introduces stability and bandwidth (or chattering) concerns that are shown to significantly constrain the selection of controller gains and actuator placements. The inclusion of

these two factors in the A-type, L-type and composite controller design is a significant contribution to the field. The contributions of this thesis are summarized as:

(i) the use of a novel fiber optic sensor array, called ShapeTape^{TM}, as an embedded feedback sensor for sensing both linear and angular deformations of the manipulator;

(ii) the design of a new controller called the composite L-type and A-type controller, and;

(iii) the procedure, based on a fundamental generalized eigenvalue problem, for determining the optimal locations and gains for each individual PZT used.

1.4 Thesis Overview

This thesis consists of six chapters. The first chapter is devoted to the objectives and the motivation behind this work. The second chapter starts with a brief introduction on dynamic modeling, and presents the Euler-Bernoulli beam model followed by the flexible link kinematics. Furthermore, the second chapter executes the derivation of the beam element dynamic equations beginning with Lagrange's equations for the beam element, as well as it does illustrate the assembly of the element equations to form the global motion equations for a 1 m long flexible link that is the subject of study in this thesis. Chapter 2 concludes with the derivations of the L-type, A-type and composite PZT control laws. These control laws are derived using the Lyapunov technique and the PZT effects are introduced as viscous damping in the global equations of motion. In Chapter 3, the actuator placement and gain selection is addressed for each PZT used by formulating a generalized eigenvalue problem from the global motion equations. The output of

Chapter 3 is a set of locations and gains. Chapter 4 focuses on the numerical simulation of the flexible link and investigates the feasibility of the control gains mathematical model developed for the flexible beam. Following Chapter 4, Chapter 5 seeks to verify the above theoretical work using a real-time experimental setup and investigates the efficacy of the proposed controllers. Concluding remarks are presented in Chapter 6.

Chapter 2 MODELING OF THE FLEXIBLE LINK

2.1 Chapter Overview

Many space structures, helicopter/rotor blades [32], turbine blades, and the flexible links of robotic manipulators can be modeled as beams. While there are beam models that account for shearing deformations of the beam cross sections, most notably those stemming from Timoshenko's beam theory, in these applications the beams' cross-sections are small in comparison to the lengths and so the classical Euler-Bernoulli theory is the most common modeling approach. The Euler-Bernoulli model assumes the beam cross section remains perpendicular to the beam centerline, but also uses fewer state variables and yields smaller, simpler system equations. Hence, the design of boundary controllers for flexible-beam-type structures has been based mainly on the Euler-Bernoulli model [25].

Figure 2.1 shows a cantilevered Euler-Bernoulli beam. One of the principle moments of inertia is very small making deflections about that axis prevalent, and bending effects

dominate the dynamics as opposed to twisting or axial effects. This feature allows simplification of a dynamics study since only a single elastic bending deformation needs to be accounted for. The bending moment at a certain point on the beam is given as [27]:

$$M(x,t) = EI(x)\frac{\partial^2 w}{\partial x^2}(x,t) \tag{2.1}$$

where E is the modulus of elasticity and $I(x)$ is the cross-sectional area moment of inertia of the variable geometry beam about the neutral axis, $w(x,t)$ is the transverse displacement of the beam, and x and t define location along the beam and time, respectively. Eq. (2.1) can be used to determine the modes of natural vibration of the beam and also the particular response to a specific external forcing. These solutions, i.e. in a clamped-free beam, depend on simple boundary conditions in a Euler-Bernoulli beam such as:

For all t, at $x = 0$: $\quad w(0,t) = 0\,, \quad \left.\dfrac{\partial w}{\partial x}\right|_0 = 0$

For all t, at $x = L$: $\quad \left.\dfrac{\partial}{\partial x}\left(EI(x)\dfrac{\partial^2 w}{\partial x^2}\right)\right|_L = 0\,, \quad \left.EI(x)\dfrac{\partial^2 w}{\partial x^2}\right|_L = 0$

In the case of flexible link dynamics, an added complication is the inertial effect introduced when the root of the beam is not static, as shown in Figure 2.1, but is rotating in a general manner. When hub motion must be considered, additional terms must be added to Eq. (2.1) to account for the time variation of the hub angle. As will be shown in this chapter, the hub rotation introduces non-linear terms which warrant a numerical solution for the Euler-Bernoulli beam deformation.

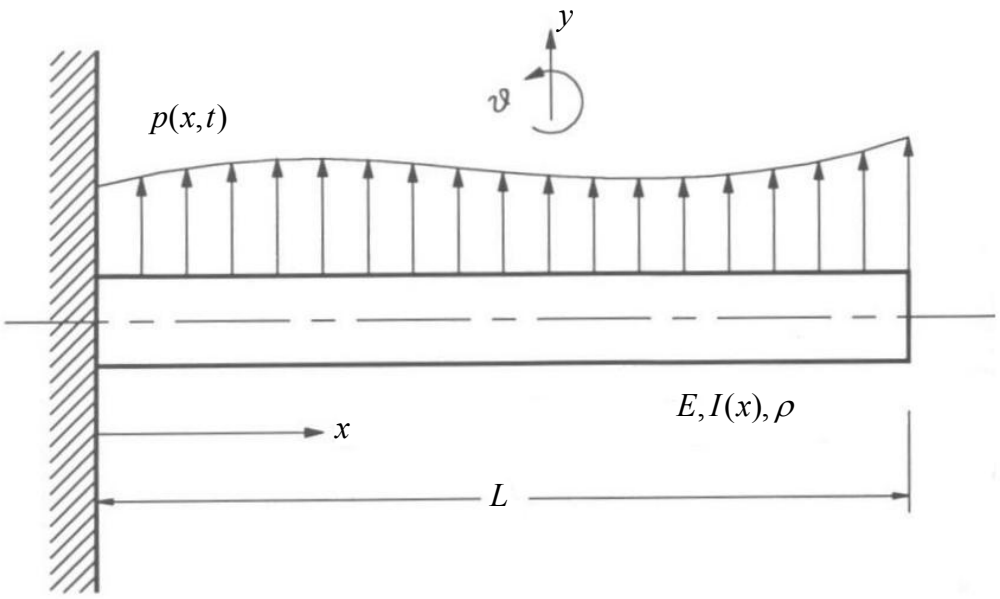

Figure 2.1 A clamped-free cantilever beam with external load

In addition, the solution of Eq. (2.1) also depends on the continuity of the beam curvature over the full domain of the analysis – the length of the flexible link. In the case of flexible robotic link addressed in this work, piezoelectric actuators will be embedded on and possibly within the flexible link. This leads to discontinuities in the internal forces and moments, and consequently the beam curvature, which compromises the classic solution to Eq. (2.1). For these reasons, the derivation of a numerical model of the beam dynamics, including elastic deformations, is necessary prior to the development of the control equations.

In this Chapter, a mathematical model based on the Euler-Bernoulli beam assumption and including hub rotation will be introduced. The Lagrange approach will be used to state the system dynamics and a finite element technique will be used to discretize the displacement field. It will be shown that the finite element formulation affords simple

inclusion of the piezoelectric actuator properties and forcing effects for those segments where the actuators are embedded. Three control laws for piezoelectric actuators will be developed using the finite element approximation to the flexible link dynamics.

2.2 Flexible Link Kinematics

The single-link flexible manipulator, shown in Figure 2.2, is modeled as a slender beam rigidly attached to a rotating hub which has two PZTs bonded on each side at a finite set of locations. Euler-Bernoulli beam theory, as explained in §2.1, is applied and axial deformation is neglected. A cubic approximation to the flexible beam's transverse elastic deflection, $w(\hat{x})$, is given in terms of a finite set of nodal variables. The transverse deflection is assumed to follow a cubic variation over each finite segment considered[17]:

$$w(\hat{x}) = a_1\hat{x}^3 + a_2\hat{x}^2 + a_3\hat{x} + a_4 \tag{2.2}$$

where $\hat{x}$ indicates axial location relative to a elemental frame located at the origin of the element. The assumed displacement field interpolates a transverse displacement, d_{iy}, and a rotation, ϕ_i, at each node of the beam element, as shown in Figure 2.2 The coefficients of Eq. (2.2) can be expressed as a function of nodal degrees of freedom, d_{1y}, d_{2y}, ϕ_1 and ϕ_2, using the following boundary conditions [17]:

$$w(0) = d_{1y} = a_4 \tag{2.3}$$

$$\left.\frac{dw(\hat{x})}{d\hat{x}}\right|_{\hat{x}=0} = \phi_1 = a_3 \tag{2.4}$$

$$w(L) = d_{2y} = a_1L^3 + a_2L^2 + a_3L + a_4 \tag{2.5}$$

$$\left.\frac{dw(\hat{x})}{d\hat{x}}\right|_{\hat{x}=L} = \phi_2 = 3a_1L^2 + 2a_2L + a_3 \tag{2.6}$$

Solving Eqs. (2.3) through (2.6) for the polynomial coefficients a_1 through a_4 and factoring the nodal degrees of freedom produces the four shape functions, N_1 through N_4 as [17]:

$$w(\hat{x},t) = [\mathbf{N}(\hat{x})]\{\mathbf{d}(t)\} \tag{2.7}$$

$$[\mathbf{N}] = [N_1, N_2, N_3, N_4]$$

$$\begin{aligned} N_1 &= \frac{1}{L^3}\left(2\hat{x}^3 - 3\hat{x}^2L + L^3\right) \quad N_2 = \frac{1}{L^3}\left(\hat{x}^3L - 2\hat{x}^2L^2 + \hat{x}L^3\right) \\ N_3 &= \frac{1}{L^3}\left(-2\hat{x}^3 + 3\hat{x}^2L\right) \qquad N_4 = \frac{1}{L^3}\left(\hat{x}^3L - \hat{x}^2L^2\right) \end{aligned} \tag{2.8}$$

and

$$\mathbf{d} = \begin{Bmatrix} d_{1y} \\ \phi_1 \\ d_{2y} \\ \phi_2 \end{Bmatrix} \tag{2.9}$$

where L denotes the length of the element, $\mathbf{N}(\hat{x})$ is the matrix of shape functions, and $\mathbf{d}(t)$ is the vector containing the nodal degrees of freedom, or generalized displacements of the link segment. One should note that the displacement field given in Eq. (2.7) is limited to small displacements relative to the length of the beam due to the lack of the axial deformation in the model which would occur with very large bending.

The absolute position at an arbitrary point along the axis of the element with respect to the global coordinate frame (XYZ) shown in Figure 2.2 is:

$$p(X,Y) = \begin{bmatrix} p_X \\ p_Y \end{bmatrix} = \begin{bmatrix} xc_\theta - w(x,t)s_\theta \\ xs_\theta + w(x,t)c_\theta \end{bmatrix} \tag{2.10}$$

where $s_\theta = \sin\theta(t)$, $c_\theta = \cos\theta(t)$ and $x = x^{(i-1)} + \hat{x}$.

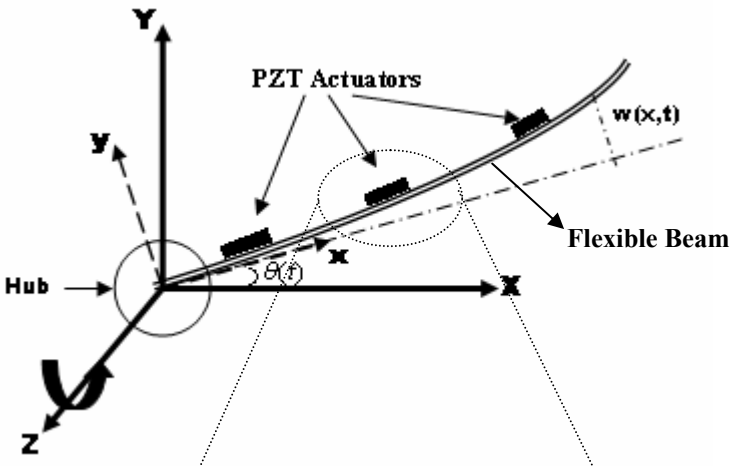

Figure 2.2.a A rotating cantilever beam

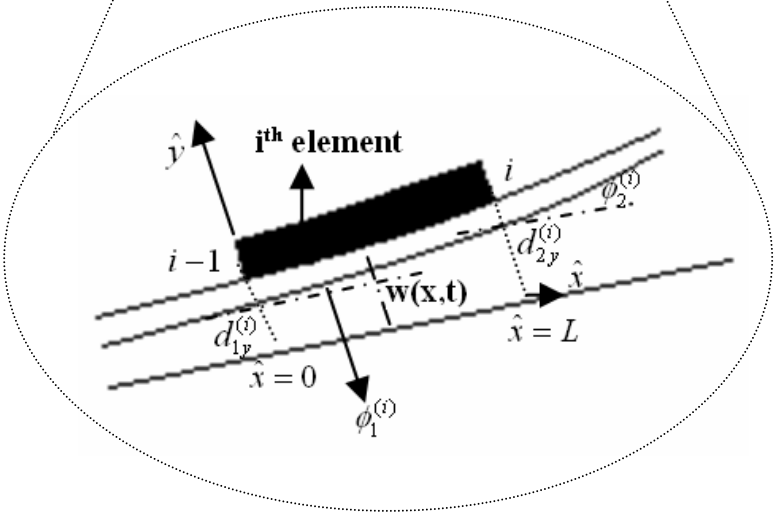

Figure 2.2.b Detailed view of a beam segment with PZT element attached

2.3 Derivation of the Beam Element Equations

The motion of the flexible link segment is a function of the entries of **d**, and the dynamics of such a multi-degree of freedom system can be defined using Lagrange's equations [29]:

$$\frac{d}{dt}\left[\frac{\partial T}{\partial \dot{q}_j}\right] - \frac{\partial T}{\partial q_j} + \frac{\partial V}{\partial q_j} = Q_j \tag{2.11}$$

where $j = 1, 2, ..., n$ indicates the particular degree of freedom, T and V are the kinetic and potential energies of the link segment, q_j and $\dot{q}_j$ are the j[th] generalized coordinate and its time differential respectively and Q_j is the generalized force associated with the q_j state variable. In the study of structures, a Lagrangian formulation is generally used due to the fact that there is a natural undeformed, or minimal energy, state to which the structure would return when it is unloaded. There are two broad classes of Lagrange formulations [10]:

(i) Updated Lagrangian (UL) formulation

(ii) Total Lagrangian (TL) formulation

In an UL formulation, the energy of the system is defined using coordinates that are relative to an evolving frame of reference. The evolving, or convected frame, is updated during a time step and solution accuracy over a single step is an accumulation of errors occurred on each update. The benefit of UL formulations is that small displacement approximations can be employed simplifying the definition of elastic strain energy. In a TL formulation, the potential energy is defined in terms of one absolute frame of

reference and the accuracy of the solution is entirely a function of how well the generalized coordinates capture the deformation, and elastic internal energy, of the system. In a TL formulation, the displacements, stresses and strains do not need transformation due to changes in the geometry of the structure [10]. In this work, it is assumed that the piezoelectric controllers will act to limit the magnitude of the elastic deformation of the flexible link, and so a simple TL formulation is used that applies a linear model of the beam deformation. It is shown in [33],that linear models of beam deformation can capture tip deflections of 20% of the link length.

For the slender beam element, the generalized displacements are the hub rotation angle, and the elemental displacement vector which contains the transverse and rotational displacements for the each edge nodes. The kinetic energy of the beam element is given as [11]:

$$T_b = \frac{1}{2}\int_0^L (\rho_b A_b + \rho_p A_p)(\dot{p}_X^2 + \dot{p}_Y^2)dx \tag{2.12}$$

where (ρ_b, A_b) and (ρ_p, A_p) denote the density and cross-section area of the beam and the perfectly bonded PZT patch, respectively. The only form of potential energy in the system is the strain energy of the beam element, which is defined by [11]:

$$U = \frac{1}{2}\int_0^L (\overline{EI})\left(\frac{\partial^2 w(x,t)}{\partial x^2}\right)^2 dx \tag{2.13}$$

where $\left(\overline{EI}\right)$ is a homogenized flexural rigidity calculated for the piezo-beam element cross section. The $\left(\overline{EI}\right)$ value accounts for the independent values of the Young's moduli, E_b and E_p, and the moments of inertia, I_b and I_p, of the beam and PZT

material about the $\hat{y}$ axis. The use of the homogeneous $\left(\overline{EI}\right)$ value assumes that the PZT patch is perfectly bonded to the surface of the beam element, and that the curvature of the beam centerline completely defines the deformation of the PZT patch. In [12], Crawley *et al.* augment the beam stiffness with an additional term created by the PZT material. In the perfectly bonded case, this stiffness is evaluated by enforcing continuity between the beam surface strain and a constant normal strain across the PZT patch. In this work, the authors extend the beam's linear strain variation across the PZT patch thickness. Substituting Eq. (2.7) into Eqs. (2.12) and (2.13), the kinetic and the strain energy equations become respectively:

$$T_b = \frac{1}{2}\int_0^L (\rho_b A_b + \rho_b A_b)\left\{(\mathbf{N}\dot{\mathbf{d}})(\mathbf{N}\dot{\mathbf{d}}) + \left[\mathrm{x}^2 + (\mathbf{N}\mathbf{d})(\mathbf{N}\mathbf{d})\right]\dot{\theta}^2 + 2(\mathbf{N}\dot{\mathbf{d}})\{x\}\dot{\theta}\right\} dx \quad (2.14)$$

$$U = \frac{1}{2}\int_0^L (\overline{EI})\left(\frac{\partial^2 \mathbf{N}(x)}{\partial x^2}\mathbf{d}\right)\left(\frac{\partial^2 \mathbf{N}(x)}{\partial x^2}\mathbf{d}\right) dx \quad (2.15)$$

Figure 2.3 shows a segment of the flexible link. The segment is subject to moments generated by the surface bonded PZT patches and to a portion of the hub torque. Following the work of Crawley et al. [12], as outlined in Appendix C, the virtual work done by the PZT layers and the hub for the perfectly bonded case can be given as:

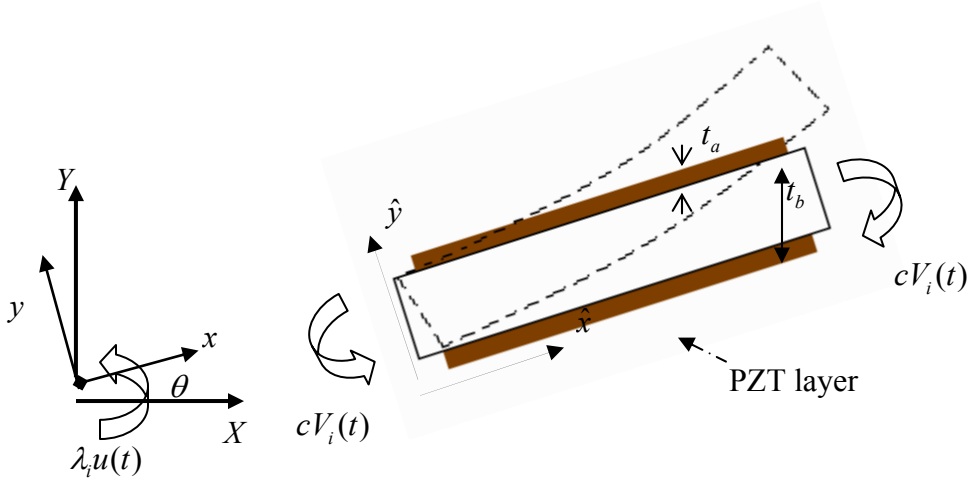

Figure 2.3. Free body diagram for the virtual work

$$\delta W = \left(\lambda_i u(t)\right)\delta\theta + \frac{cV_i(t)\delta\theta}{2} - \frac{cV_i(t)\delta\theta}{2} + cV_i(t)\left\{\delta\phi_2 - \delta\phi_1\right\} \tag{2.16}$$

where $cV_i(t)\left\{\delta\phi_2 - \delta\phi_1\right\} = cV_i(t)\left\{\mathbf{N}'(L) - \mathbf{N}'(0)\right\}\delta\mathbf{d}$ which leads to:

$$\delta W = \underbrace{\left(\lambda_i u(t)\right)\delta\theta + \frac{cV_i(t)\delta\theta}{2} - \frac{cV_i(t)\delta\theta}{2}}_{\delta W_\theta} + \underbrace{cV_i(t)\left\{\mathbf{N}'(L) - \mathbf{N}'(0)\right\}\delta\mathbf{d}}_{\delta W_d} \tag{2.17}$$

where $V(t)$ is the applied voltage to the actuator, $\lambda_i u(t)$ is the portion of the input torque delivered to the the i^{th} element by the hub (where $0 < \lambda_i < 1$) and the product $cV_i(t)$ is the magnitude of the bending moment, m_i, generated by the surface bonded PZT patches:

$$m_i = cV_i(t) \tag{2.18}$$

In equation (2.18), c is a constant scalar defined as [18]:

$$c = \frac{1}{2}E_a d_{31} w_a (t_a + t_b) \tag{2.19}$$

and d_{31} is the dielectric constant for actuators, w_a and t_a are the width and thickness of the actuators, t_b is the thickness of the beam and E_a denotes Young's modulus of the PZT.

Given Eqs. (2.14), (2.15) and (2.17), the Total Lagrangian formulation for the combined piezo-beam element can be given as:

$$\frac{d}{dt}\left[\frac{\partial T}{\partial \dot{\mathbf{d}}}\right]-\frac{\partial T}{\partial \mathbf{d}}+\frac{\partial U}{\partial \mathbf{d}}=\mathbf{Q}_d \quad \text{and} \quad \frac{d}{dt}\left[\frac{\partial T}{\partial \dot{\theta}}\right]-\frac{\partial T}{\partial \theta}+\frac{\partial U}{\partial \theta}=Q_\theta \tag{2.20}$$

where $\mathbf{Q}_d\delta\mathbf{d}=\delta W_d$ and $\mathrm{Q}_\theta\delta\theta=\delta W_\theta$ and the individual terms of the Eq. (2.20) become:

$$\frac{d}{dt}\left[\frac{\partial T}{\partial \dot{\mathbf{d}}}\right]=(\rho_b A_b+\rho_p A_p)\int_0^L \mathbf{N}^T\mathbf{N}dx\ddot{\mathbf{d}}+(\rho_b A_b+\rho_p A_p)\int_0^L \mathbf{N}xdx\ddot{\theta} \tag{2.21}$$

$$\frac{\partial T}{\partial \mathbf{d}}=(\rho_b A_b+\rho_p A_p)\int_0^L \mathbf{N}^T\mathbf{N}dx\dot{\mathbf{d}}\dot{\theta}^2 \tag{2.22}$$

$$\frac{\partial U}{\partial \mathbf{d}}=(\overline{EI}\int_0^L (\mathbf{N}'')^T(\mathbf{N}'')dx)\mathbf{d} \tag{2.23}$$

$$\frac{d}{dt}\left[\frac{\partial T}{\partial \dot{\theta}}\right]=(\rho_b A_b+\rho_p A_p)\left[2\mathbf{d}^T\int_0^L \mathbf{N}^T\mathbf{N}dx\dot{\mathbf{d}}\dot{\theta}+\underline{d}^T\int_0^L \mathbf{N}^T\mathbf{N}dx\mathbf{d}\ddot{\theta}+\int_0^L x^2dx\ddot{\theta}+\int_0^L \mathbf{N}xdx\ddot{\mathbf{d}}\right] \tag{2.24}$$

$$\frac{\partial T}{\partial \theta}=0 \quad \text{and} \quad \frac{\partial U}{\partial \theta}=0 \tag{2.25}$$

Factoring Eqs. (2.21) through (2.25) in a matrix form produces:

$$\begin{bmatrix}\mathbf{M} & \mathbf{A}\\ \mathbf{A}^{\mathbf{T}} & \mathbf{d}^{\mathbf{T}}\mathbf{M}\mathbf{d}+D\end{bmatrix}_{5\times5}\begin{bmatrix}\ddot{\mathbf{d}}\\ \ddot{\theta}\end{bmatrix}_{5\times1}+\begin{bmatrix}\mathbf{0} & -\mathbf{M}\dot{\boldsymbol{\theta}}\mathbf{d}\\ \dot{\boldsymbol{\theta}}\mathbf{d}^{\mathbf{T}}\mathbf{M} & \mathbf{d}^{\mathbf{T}}\mathbf{M}\dot{\mathbf{d}}\end{bmatrix}_{5\times5}\begin{bmatrix}\dot{\mathbf{d}}\\ \dot{\theta}\end{bmatrix}_{5\times1}+\begin{bmatrix}\mathbf{K}\\ 0\end{bmatrix}_{5\times5}\begin{bmatrix}\mathbf{d}\\ \theta\end{bmatrix}_{5\times1}=\begin{bmatrix}\mathbf{F}\\ \lambda_i u(t)\end{bmatrix}_{5\times1} \tag{2.26}$$

where:

$$\mathbf{M} = (\rho_b A_b + \rho_p A_p)\int_0^L \mathbf{N}^T \mathbf{N} dx \tag{2.27}$$

$$\mathbf{K} = (\overline{EI})\int_0^L (\mathbf{N}'')^T (\mathbf{N}'') dx \tag{2.28}$$

$$\mathbf{A} = (\rho_b A_b + \rho_p A_p)\int_0^L \mathbf{N}^T x dx \tag{2.29}$$

$$D = (\rho_b A_b + \rho_p A_p)\int_0^L x^2 dx \tag{2.30}$$

$$\mathbf{F} = m_i(t)\left[\mathbf{N}'^T(L) - \mathbf{N}'^T(0)\right] \tag{2.31}$$

2.4 Assembly of the Flexible Link Model

The model of the entire flexible beam is formed by assembling a series of the piezo-beam element equations given by Eq. (2.26). For those beam elements that have no surface bonded PZT patches domains of the assembly where the PZT is absent, A_p in the corresponding element equations is set to zero. The assembled (global) motion equation of the beam is given by:

$$\underbrace{\begin{bmatrix} \mathbf{M}_G & \mathbf{A}_G \\ \mathbf{A}_G^T & Q \end{bmatrix}}_{Mf}_{(2n-1)\times(2n-1)} \begin{bmatrix} \ddot{\mathbf{d}}_G \\ \ddot{\theta} \end{bmatrix}_{(2n-1)\times 1} + \underbrace{\begin{bmatrix} \mathbf{0} & -\mathbf{M}_G\dot{\theta}\mathbf{d}_G \\ \dot{\theta}\mathbf{d}_G^T\mathbf{M}_G & \mathbf{d}_G^T\mathbf{M}_G\dot{\mathbf{d}}_G \end{bmatrix}}_{Cf}_{(2n-1)\times(2n-1)} \begin{bmatrix} \dot{\mathbf{d}}_G \\ \dot{\theta} \end{bmatrix}_{(2n-1)\times 1}$$
$$+ \begin{bmatrix} \mathbf{K}_G \\ 0 \end{bmatrix}_{(2n-1)\times(2n-1)} \begin{bmatrix} \mathbf{d}_G \\ \theta \end{bmatrix}_{(2n-1)\times 1} = \begin{bmatrix} \mathbf{F}_G \\ u(t) \end{bmatrix}_{(2n-1)\times 1} \tag{2.32}$$

where $Q = \sum_{i=1}^{2n-1} \mathbf{d}_i^T \mathbf{M}_i \mathbf{d}_i + D_i$. This assembly of equations has two distinct components: the top row is a set of $(2n)$ equations defining the evolution of the state variables $\mathbf{d}_G$ which define the elastic deformation of the flexible link. The bottom row governs the evolution of the hub angle θ. However, one should keep in mind that the first two degrees of freedom within $\mathbf{d}_G$ can be eliminated from the global assembled system since the beam is clamped at the hub and the transverse and rotational elastic displacement of the very first node are assured to be zero. Hence, the global assembled system has $(2n-1)$ degrees of freedom.

If ${m^{(n)}}_{ij}$ and ${k^{(n)}}_{ij}$ are the ij^{th} entry of the n^{th} element's mass and stiffness matrices respectively, then the global mass and stiffness matrix excluding the boundary conditions can be given as:

$$\mathbf{M}_G = \begin{bmatrix} {m^{(1)}}_{11} & {m^{(1)}}_{12} & {m^{(1)}}_{13} & {m^{(1)}}_{14} & 0 & 0 & \cdots & \cdots & \cdots & 0 \\ {m^{(1)}}_{11} & {m^{(1)}}_{11} & {m^{(1)}}_{11} & {m^{(1)}}_{24} & 0 & 0 & & & & \\ {m^{(1)}}_{11} & {m^{(1)}}_{11} & {m^{(1)}}_{11} + {m^{(2)}}_{11} & {m^{(1)}}_{34} + {m^{(2)}}_{12} & {m^{(2)}}_{13} & {m^{(2)}}_{14} & & & & \\ {m^{(1)}}_{11} & {m^{(1)}}_{11} & {m^{(1)}}_{11} + {m^{(2)}}_{21} & {m^{(1)}}_{44} + {m^{(2)}}_{22} & {m^{(2)}}_{23} & {m^{(2)}}_{24} & & & & \\ 0 & 0 & {m^{(2)}}_{31} & {m^{(2)}}_{32} & {m^{(2)}}_{33} + {m^{(3)}}_{11} & {m^{(2)}}_{34} + {m^{(3)}}_{12} & & & & \\ 0 & 0 & {m^{(2)}}_{41} & {m^{(2)}}_{42} & {m^{(2)}}_{43} + {m^{(3)}}_{21} & {m^{(2)}}_{44} + {m^{(3)}}_{22} & & & & \\ \vdots & & & & & & \ddots & & & \\ \vdots & & & & & & & \ddots & & \\ \vdots & & & & & & & & \ddots & \\ 0 & & & & & & & & & {m^{(i)}}_{44} \end{bmatrix}_{(2n)\times(2n)} \tag{2.33}$$

$$\mathbf{K}_G = \begin{bmatrix} k^{(1)}{}_{11} & k^{(1)}{}_{12} & k^{(1)}{}_{13} & k^{(1)}{}_{14} & 0 & 0 & \cdots & \cdots & \cdots & 0 \\ k^{(1)}{}_{11} & k^{(1)}{}_{11} & k^{(1)}{}_{11} & k^{(1)}{}_{24} & 0 & 0 & & & & \\ k^{(1)}{}_{11} & k^{(1)}{}_{11} & k^{(1)}{}_{11}+k^{(2)}{}_{11} & k^{(1)}{}_{34}+k^{(2)}{}_{12} & k^{(2)}{}_{13} & k^{(2)}{}_{14} & & & & \\ k^{(1)}{}_{11} & k^{(1)}{}_{11} & k^{(1)}{}_{11}+k^{(2)}{}_{21} & k^{(1)}{}_{44}+k^{(2)}{}_{22} & k^{(2)}{}_{23} & k^{(2)}{}_{24} & & & & \\ 0 & 0 & k^{(2)}{}_{31} & k^{(2)}{}_{32} & k^{(2)}{}_{33}+k^{(3)}{}_{11} & k^{(2)}{}_{34}+k^{(3)}{}_{12} & & & & \\ 0 & 0 & k^{(2)}{}_{41} & k^{(2)}{}_{42} & k^{(2)}{}_{43}+k^{(3)}{}_{21} & k^{(2)}{}_{44}+k^{(3)}{}_{22} & & & & \\ \vdots & & & & & & \ddots & & & \\ \vdots & & & & & & & \ddots & & \\ \vdots & & & & & & & & \ddots & \\ 0 & & & & & & & & & k^{(n)}{}_{44} \end{bmatrix}_{(2n)\times(2n)} \tag{2.34}$$

Finally, $\mathbf{A}$ in Eq. (2.26), which is the mass distribution matrix over the length of the flexible beam, can be given by:

$$\mathbf{A}_G = \begin{bmatrix} a_{11}^{(1)} & a_{12}^{(1)} & a_{13}^{(1)}+a_{11}^{(2)} & a_{14}^{(1)}+a_{12}^{(2)} & a_{13}^{(2)} & a_{14}^{(2)} & \cdots & \cdots & \cdots & a_{14}^{(n)} \end{bmatrix} \tag{2.35}$$

2.5 Hybrid Control of Slewing Maneuvers

In this thesis, a stability analysis depending on Lyapunov's direct method is presented using the dynamic model of the assembled flexible link given in the previous section. The primary concern is the use of the piezoelectric patches for suppression of vibrations in an effective yet stable manner. However, the vibration suppression must occur in the presence of a hub controller which ensures the flexible link completes the desired slewing maneuver. The overall system control is hereafter referred to as hybrid control of the flexible link. As will be shown in subsequent chapters, both the hub and piezoelectric components of the hybrid controllers work to keep the link deformation within the realm of linear elasticity.

2.5.1 Lyapunov's Direct Method

By definition, Lyapunov's direct method for stability indicates that if a controller can ensure that the total energy of a mechanical (or electrical) system is continuously dissipated, then the system, whether linear or nonlinear, must eventually settle to an equilibrium configuration [21]. A scalar function that quantifies the system energy, called a Lyapunov function candidate, is used to monitor the stability of the system. If there exists a scalar function V of the state x, with continuous first order derivatives such that:

(i) $V(x)$ is positive definite ($V(x) > 0$),

(ii) $\dot{V}(x)$ is negative semi-definite ($\dot{V}(x) \leq 0$),

then an equilibrium configuration defined by $V = 0$ is stable.

The significant difficulty in implementing Lyapunov's direct method for controller synthesis is the selection of a function candidate in terms of the system state variables. Provided a proper function, it then remains only to ensure that the control law ensures the two conditions listed above. If the controller's objective is to eliminate unwanted motion and elastic deformation, as is the case in this work, then a function indicative of the kinetic and potential energies of the system is usually selected. However, additional terms must also be considered to ensure that the desired systems motions are identified and accomplished by the controller [25].

For the flexible link shown in Figure 2.2, a suitable Lyapunov function candidate can be chosen as follows [21]:

$$V = \frac{1}{2}[\dot{\mathbf{x}}^T \mathbf{M}_\mathbf{f} \dot{\mathbf{x}} + \mathbf{d}^T \mathbf{K} \mathbf{d} + k_p \Delta\theta^2] \tag{2.36}$$

where $\Delta\theta = \theta - \theta_d$ is the position error of the hub angle, θ_d denotes the desired hub angle, k_p is the proportional gain on the angular displacement of the hub, and $\mathbf{x} = \begin{bmatrix} \mathbf{d}_G & \theta \end{bmatrix}^T$. The first term on the right side of Eq. (2.36) represents the kinetic energy of the system and the second term represents the strain energy of the flexible link. The last term denotes the potential energy associated with the hub rotation, which can be interpreted as an artificial torsional spring [21]. The third term of Eq. (2.36) is the hub control contribution and is a heuristic component intended to ensure that the flexible link completes the desired slewing maneuvers regardless of any piezoelectric activity.

Rather than taking the time derivative of Eq. (2.36) explicitly, conservation of energy is applied, as is shown in [21], and the rate of change of the kinetic and strain energies in the system is equated to the power provided by external forces. This yields for a finite length segment:

$$\dot{V} = \begin{bmatrix} \dot{\mathbf{d}} \\ \dot{\theta} \end{bmatrix}^T \begin{bmatrix} \mathbf{F} \\ u(t) \end{bmatrix} + \dot{\theta}\, k_p \Delta\theta \tag{2.37}$$

which can be rewritten as:

$$\dot{V} = \dot{\theta}(u(t) + k_p \Delta\theta) + \dot{\mathbf{d}}^T \mathbf{F} \tag{2.38}$$

where k_p is the proportional gain on the angular displacement (θ) of the hub. In Eq. (2.38), the input torque from the hub, $u(t)$, is defined using a PD control law:

$$u(t) = -k_p \Delta\theta - k_v \dot{\theta} \tag{2.39}$$

where k_v is the derivative gain on the angular velocity ($\dot{\theta}$) of the hub. Applying Eq. (2.39) to Eq. (2.38) yields:

$$\dot{V} = -k_v \dot{\theta}^2 + \dot{\mathbf{d}}^T \mathbf{F} \tag{2.40}$$

If one can show that Eq. (2.40) is negative semi-definite (i.e. $\dot{V}(x) \le 0$), the stability criterion is satisfied. It can easily be noted that for $k_V > 0$, the first term on the right side of Eq. (2.40) is less than or equal to zero. The second term represents the impact of the PZTs on the stability of the flexible link. Substituting Eq. (2.32) into Eq.(2.40), we obtain:

$$\dot{V} = -k_v \dot{\theta}^2 + \dot{\mathbf{d}}^T c V_i(t) \left\{ N'^T(L) - N'^T(0) \right\} \tag{2.41}$$

Then, the substitution of Eq. (2.7) into Eq. (2.41) leads to:

$$\dot{V} = -k_V \dot{\theta}^2 + \dot{\mathbf{d}}^T c V_i(t) \left\{ \dot{w}'^T(L,t) - \dot{w}'^T(0,t) \right\} \tag{2.42}$$

where $\dot{(\ )}$ denotes the differentiation of $(\ )$ with respects to time and $(\ )'$ denotes the differentiation of $(\ )$ with respects to displacement; therefore, $\dot{w}'(L,t) - \dot{w}'(0,t)$ denotes the angular velocity difference between the two nodes of the PZT element.

2.5.2 A-Type Controller

It can easily be shown that, if the control voltage of the i^{th} piezo element, $V_i(t)$, is chosen as:

$$V_i(t) = -k_A \left[\dot{w}_i'(L,t) - \dot{w}_i'(0,t) \right] \tag{2.43}$$

then Eq. (2.42) becomes:

$$\dot{V} = -k_V \dot{\theta}^2 - ck_A \left[\dot{w}_i'(L,t) - \dot{w}_i'(0,t)\right]^2 \tag{2.44}$$

and $\dot{V} \le 0$ for all possible system states provided c is a positive material property (which is always true) and $k_A > 0, k_V > 0$. In other words, the Lyapunov condition for stability is satisfied, energy of the system will be dissipated and vibration of the flexible link will be suppressed.

The control law given in Eq. (2.43) is referred to hereafter as an A-type control strategy as it depends on angular velocity feedback. As mentioned previously, by using the array of fiber optic sensors we can acquire the angular velocity data needed to realize the A-type controller. In previous works angular velocity was not considered to be a realistic feedback signal [1].

2.5.3 L-Type Controller

The use of translational velocities as feedback, here referred to as L-type control, was previously proposed in [1] and was motivated by the practical drawback of acquiring the angular velocity data in the past. In the L-type control strategy, the control voltage is:

$$V_i(t) = -k_L \left[\dot{w}_i(L,t) - \dot{w}_i(0,t)\right] \tag{2.45}$$

Substituting Eq. (2.45) into Eq. (2.42) leads to:

$$\dot{V} = -k_V \dot{\theta}^2 - ck_L \left[\dot{w}_i'(L,t) - \dot{w}_i'(0,t)\right]\left[\dot{w}_i(L,t) - \dot{w}_i(0,t)\right] \tag{2.46}$$

Examining Eq. (2.46) one should note that $\dot{V} \le 0$ is not always guaranteed. Thus the use of the control law in Eq. (2.46) does not always satisfy the Lyapunov condition, and

instabilities may result in controlling the link vibration using the L-type controller. The stability of the L-type controller is a function of the PZT actuator placements and this problem was studied in detail by Sun et al. [1]. The proposed placement strategy is to place the actuators along the link in a way to ensure that the actuators are away from the regions where the second derivatives of the shape functions change signs. In other words, if the actuators are placed on the regions where the surface strain does not change its sign, then stability will be ensured. In order to satisfy this condition, the actuators can be placed towards the tip or root of the link [1]. One should note that the choice of a large hub gain k_V and/or conservative hub motions can also ensure stability. Furthermore, the selection of PZT locations in [1] is completed considering the first few natural modes of vibration [1]. However, one should note that the PZT actuators introduce significant non-proportional system damping and that leads these modes to be perturbed. Hence, the choice made dependent on those natural modes may not be trustworthy.

2.5.4 The Composite Controller

Since both the angular and linear velocity feedback data are available using the fiber optic sensor array, one can develop a composite control strategy, which is the superposition of the A-type and L-type controllers:

$$V_i(t) = -k_L\left[\dot{w}_i(L,t) - \dot{w}_i(0,t)\right] - k_A\left[\dot{w}_i'(L,t) - \dot{w}_i'(0,t)\right] \tag{2.47}$$

With this composite controller, one can compensate for the unstable tendencies of the L-type that occur when the PZT actuators are placed such that Sun's general rules aren't

satisfied. In addition, in §4.5 the composite controller will be shown to be more effective in suppressing beam vibration than either the A-type or L-type controllers alone.

As previously mentioned, a simple PD-based hub controller (given in Eq. (2.39)) is always present. The hub controller not only creates the slewing maneuver of the link, but it also actively contributes in suppressing the link vibration and avoiding any undesired large tip deflections. This is due to the centrifugal stiffening added to the system by the slewing maneuver. As can be seen in the Eq. (2.32), there is no viscous or coulomb damping in the system present. However; the generalized force provided by the hub does create a viscous component due to its dependence on $\dot{\theta}$ and this viscous force affects the elastic displacement of the flexible link through the matrix of coriolis terms – the second matrix on the left hand side of Eq. (2.32). Therefore, the hub controller is expected to contribute to the suppression of the link vibration, and this is seen in both the simulation results of §4 and the experimental results of §5.

2.6 Piezo-Element Damping

To quantify the system stability, the control strategy of Eq. (2.47) must be amalgamated with the element equations given within Eq. (2.26). To isolate the PZT controller performance, the rotational hub motion is eliminated and a clamped-free case is taken into consideration. In the absence of the hub rotation, $\theta = \dot{\theta} = \ddot{\theta} = 0$, and the element motion equations, Eq. (2.26), reduce to a series of 4 undamped second order differential equations in terms of the element state variables:

$$\mathbf{M}\ddot{\mathbf{d}} + \mathbf{K}\mathbf{d} = \mathbf{F} \tag{2.48}$$

If PZT patches are bonded to the beam element surfaces then $A_p \neq 0$, $m_i = cV_i \neq 0$ and for the case of the composite controller the piezo voltage is given by Eq. (2.47). Applying the shape functions defined in Eq. (2.8), the constant bending moment generated across the piezo-beam element is given by:

$$\begin{aligned} m_i &= -c\left(k_L\left[\dot{w}_i(L,t)-\dot{w}_i(0,t)\right]+k_A\left[\dot{w}_i'(L,t)-\dot{w}_i'(0,t)\right]\right) \\ &= -c\left(k_L\left[\dot{d}_{2y}-\dot{d}_{1y}\right]+k_A\left[\dot{\phi}_2-\dot{\phi}_1\right]\right) \end{aligned} \tag{2.49}$$

Substituting Eq. (2.49) into the elemental force matrix $\mathbf{F}$ given in Eq. (2.31) yields a state dependent load:

$$\mathbf{F} = -\mathbf{C}\dot{\mathbf{d}} \tag{2.50}$$

where,

$$\mathbf{C} = \begin{bmatrix} 0 & 0 & 0 & 0 \\ -G_L & -G_A & G_L & G_A \\ 0 & 0 & 0 & 0 \\ G_L & G_A & -G_L & -G_A \end{bmatrix} \tag{2.51}$$

and the gains G_L and G_A represents the L-type and A-type components of the composite controller in the damping matrix and include contributions of the piezo constant, *c*, and the control gains k_L and k_A, respectively:

$$\begin{aligned} G_L &= ck_L \\ G_A &= ck_A \end{aligned}$$

Using Eq. (2.50) in Eq. (2.48) yields:

$$\mathbf{M}\ddot{\mathbf{d}} + \mathbf{C}\dot{\mathbf{d}} + \mathbf{K}\mathbf{d} = \mathbf{0} \tag{2.52}$$

In Eq. (2.52) it is apparent that the PZT control is the only source of viscous damping when the hub is locked. In the next chapter, the clamped free case encapsulated by Eq. (2.52) will be used in the selection of feedback gains G_A and G_L and actuator locations since it is the worst case scenario – there is no hub activity to compensate poor piezoelectric control performance.

Chapter 3 ACTUATOR PLACEMENT AND GAIN SELECTION

3.1 Chapter Overview

Existing works have shown that the use of multiple PZT actuators improves the dissipation of beam vibrations in both clamped [2-4] and slewing maneuvers [1,5,7]. However, the placement of these actuators and the specification of their individual gains is an important factor that affects the final controller performance. While many of the previous works have made provision for independent gains k_A and k_L in the formulation stage, the implementation of the controller generally occurs with uniform gains across the system [1, 3]. Here, we attempt to provide a procedure that can be used to produce more stringent bounds on the PZT gains than $k_A > 0$ and $k_L > 0$: bounds that reflect stability considerations and the limits of the piezo-actuators' bandwidth.

3.2 Methodology

In choosing the location of a PZT patch, and its gain values k_A and k_L, the non-proportional nature of the system must be considered. To date, non-proportionally damped systems have been examined outside of the vibration control field [22, 23]. The focus of both [22] and [23], is the response of linear lumped parameter systems. Such systems can be easily represented in standard state space form from which the associated eigenproblem can be solved through either a single global solution [22], or sub-structuring of the original problem through the application of appropriate boundary conditions between the sub-domains [23].

Of particular relevance to this work, Sorrentino et al. demonstrated in [23, pp. 776-777], that non-proportional contributions to system damping may not significantly affect the lower, or fundamental, mode of vibration but can lead to instabilities in the higher modes of vibration. The existence of a critical level of damping for the higher modes indicates that there must be an upper bound on the values of the gains k_A and k_L.

In the vibration control field, an assumed mode method is most often used to model the beam deformation and produce the system of equations defining the evolution of the modal amplitudes [1, 12]. However, in [12] only the fundamental mode is considered, and a 1-DOF equation defining the evolution of this fundamental mode results. In this case, the damping provided by the PZT patches is inherently proportional, and increasing the gains on the PZT voltage can not possibly increase the frequency of vibration or create instabilities. This is in stark contrast to the results of [23]. In [1], the first six natural modes of the system are used to create a discrete system model using a Ritz

technique. Integrating that model in time, the modal magnitudes will develop such that asynchronous node motions occur and hence the non-proportional nature of the piezoelectric patches is captured. However, between the modeling and control design stages of [1] there is a theoretical disconnect – the placement of the PZT patches is completed based on three conditions established on the system's natural modes themselves. These conditions do not account for the significant non-proportional damping exerted by the PZT patches and how this non-proportional damping alters the natural tendencies. While the results in [1] demonstrate stability, this stability is heavily dependent on a final heuristic placement and gain selection – a consequence of the non-proportionality not appearing quantitatively in the design process.

In stark contrast to predictions stemming from a proportional analysis, this section will show that increases in the controller gains do not necessarily translate to improved damping behavior. In fact, large gain values can lead to system instabilities and undesirable chattering of the PZT patches.

3.3 The Generalized Eigen-Value Problem

The cantilevered beam is modeled by assembling the element equations of Eq. (2.52). For standard beam elements, those without surface bonded PZT patches, in the assembly $A_p = 0$ and $\mathbf{C} = \mathbf{0}$. This assembly process follows the serial connection of elements outlined in Eq. (2.33) and Eq. (2.34) and yields:

$$\mathbf{M}_G \ddot{\mathbf{d}}_G + \mathbf{C}_G \dot{\mathbf{d}}_G + \mathbf{K}_G \mathbf{d}_G = \mathbf{0} \tag{3.1}$$

where $\mathbf{M}_G, \mathbf{C}_G$ and $\mathbf{K}_G$ are the global mass, damping and the stiffness matrices respectively and $\mathbf{d}_G$ is the global state vector as defined in Eq. (2.32). The damping matrix in Eq. (3.1) is inherently non-proportional since the PZT patches produce opposing moments at the element ends which yields the non-symmetric **C** in Eq. (2.51). The non-proportional damping makes the natural modes of vibration in the system inseparable, and the response to any initial disturbance of the cantilevered beam will be a blend of asynchronous complex modes rather than the natural modes of the piezo-beam assembly. In a proportionally damped system, the modes are separable and the damping matrix can be given proportional to mass and stiffness matrices where as this is not the case for a non-proportionally damped system.

The k^{th} possible solution to Eq. (3.1), is known to be of a form:

$$\mathbf{d}_G = \mathbf{D}_k e^{(a_k + ib_k)t} \tag{3.2}$$

where $\mathbf{D}_k$ is a matrix of complex amplitudes of the assembled system's state variables, a_k defines the growth or attenuation of the response, b_k defines the cyclic frequency of the oscillations and the integer k denotes the k^{th} mode of response. Depending on the strength of the non-proportional terms in $\mathbf{C}_G$, the modes of Eq. (3.1) will be comparable to the natural modes of the assembled system. The accuracy of the predicted k^{th} mode depends on the discretization scheme: higher order modes can only be resolved with the use of a large number of elements.

Substituting Eq. (3.2) into Eq. (3.1) produces a Generalized Eigenvalue Problem (here after referred as GEP). A GEP technique from [24] is outlined in Appendix A, and this

technique yields the system eigenvalues, $a_k + ib_k$. By considering the non-proportional nature of $\mathbf{C}_G$, we allow for the possibility that $a_k > 0$ - an instability due strictly to the L-type piezo control method given in Eq. (2.45).and in Eq. (2.47).

Since the primary design consideration is stability, we choose to use the envelope bounding the beam oscillations as a performance criterion for the controllers. For all modes that are believed to be accurately captured by the discretization scheme, the controller gains must yield:

$$a_k < 0 \tag{3.3}$$

In most cases, it is expected that the magnitude of the higher order vibrations will be small. But if these fast vibrations persist, or grow, on top of the overall slewing maneuver, the task intensity increases and the vibrations could appear as Gaussian noise in the final hardware setup.

As the rate of decay gets larger; the duration of the suppression is expected to shorten. However, by analogy to simple 1-DOF systems, the rate of decay of the oscillations can also be directly related to the natural frequency of the vibration – a value that rises as the controller gains are raised and the stiffness of the system increases. Hence, situations where $a_k << 0$ are expected with the use of extremely large and unrealistic choices of k_L and k_A. In short, the larger gains yield higher voltages and larger restoring moments for the same deformation. This raises the stiffness of the system and increases the frequency of the vibration – an effect commonly referred to as chatter. To avoid chatter we must bound the control gains on the high side. This is done by ensuring that:

$$b_k < \omega_k \tag{3.4}$$

where ω_k is the k^{th} natural frequency of the assembled piezo-beam. The inequality of Eq. (3.4) presumes that the non-proportional damping does not cause the modal frequencies to crossover. In this work, it is proposed that situations where $b_k \geq \omega_k$ be referred to as chattering.

In the design of the controlled beam slewing maneuver, three PZT elements are to be distributed over the beam. We propose to dedicate each PZT to the control of a specific lower order mode of vibration. Since the first three modes of vibration in a real time application are generally the modes that can be excited, these modes were taken into consideration to complete the procedure. The location and gain of each individual PZT is optimized by considering how location and gain choices affect the two criteria of Eq. (3.3) and Eq. (3.4) for $1 \leq k \leq 3$.

3.4 Results

Having removed the hub, the clamped-free piezo-beam having 7 segments (14 DOF) and only one actuator, as depicted in Figure 3.1 is assembled. The effect of actuator placement and gains selection on each mode has been observed by incrementally sliding the PZT segment between the hub and the tip. At each step, the $k_L = \frac{G_L}{c}$ and $k_A = \frac{G_A}{c}$ gains are varied over all possible combinations within the ranges $0 \leq k_A \leq 10^4$ V-sec/rad and $0 \leq k_L \leq 10^4$ V-sec/rad. For each combination of k_A and k_L, the values of a_k and b_k

are computed. From the computed results, the $a_k = 0$ and $b_k = \omega_k$ contours can be extracted. Given that the model possesses 14 nodal degrees of freedom, only the first ten modes, $1 \le k \le 10$, are considered. The results are as indicated in Figures 3.2 through 3.7:

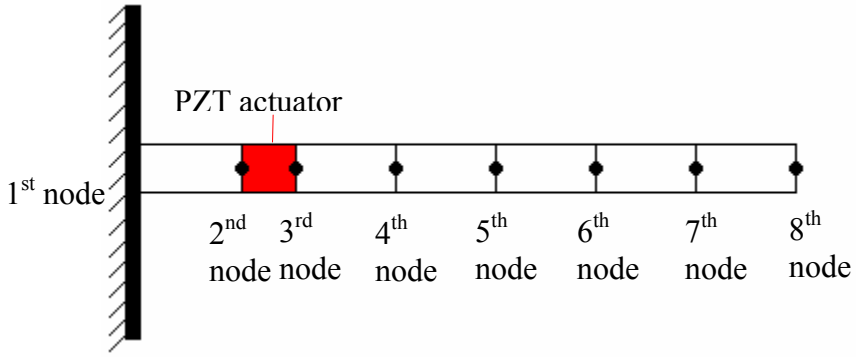

Figure 3.1. Clamped-free cantilever beam with a PZT actuator on the second element

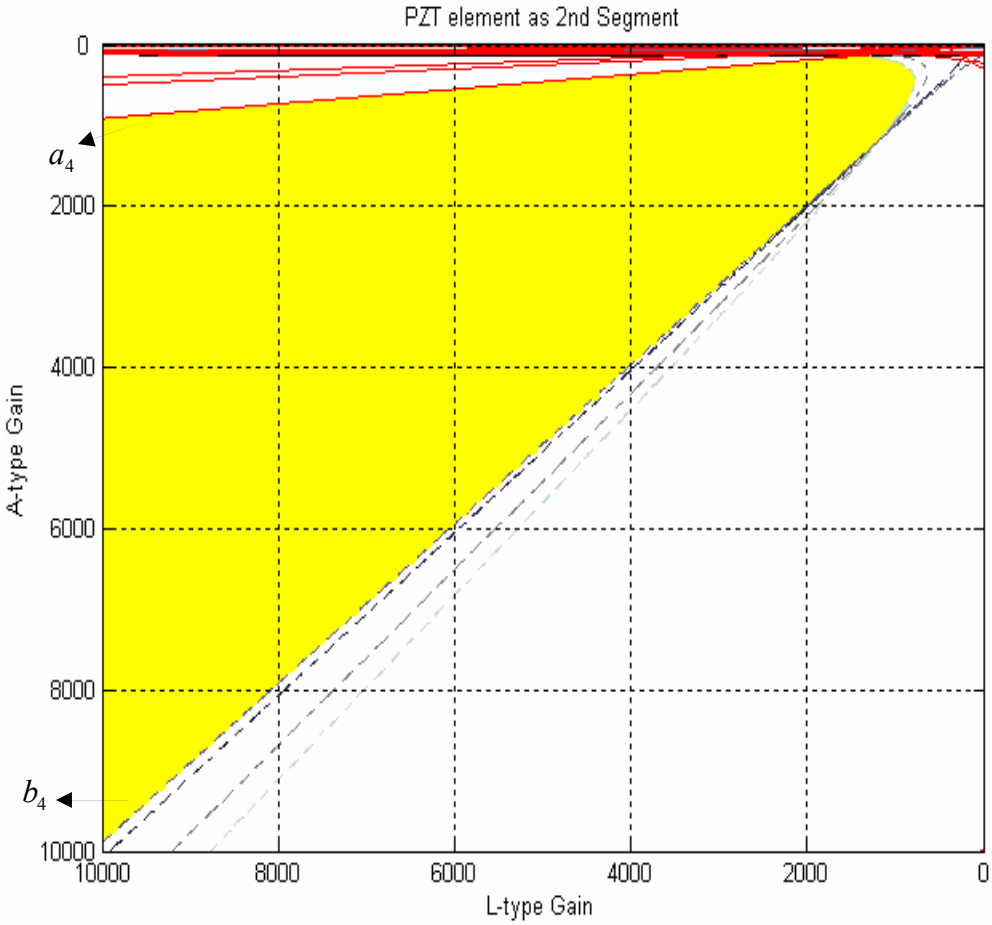

Figure 3.2. Feasible regions for the controller gains-PZT element as 2nd Segment

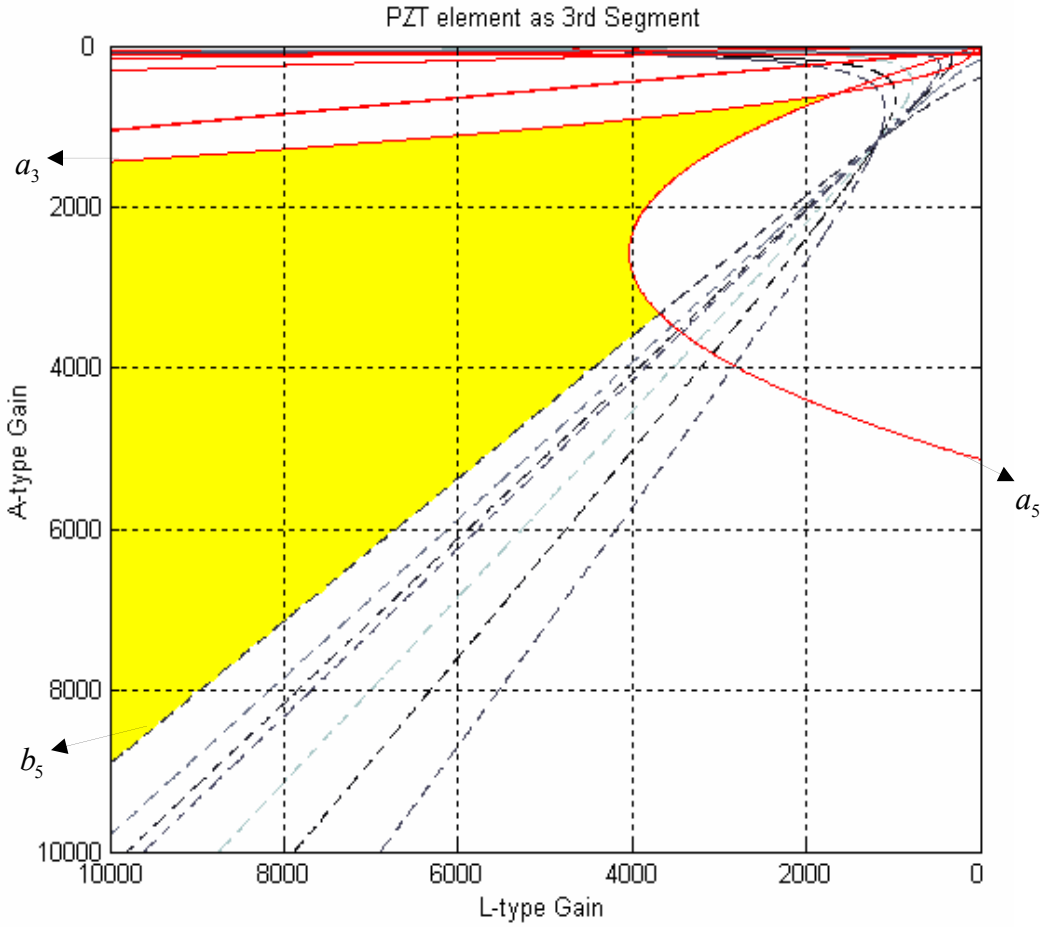

Figure 3.3. Feasible regions for the controller gains-PZT element as 3rd Segment

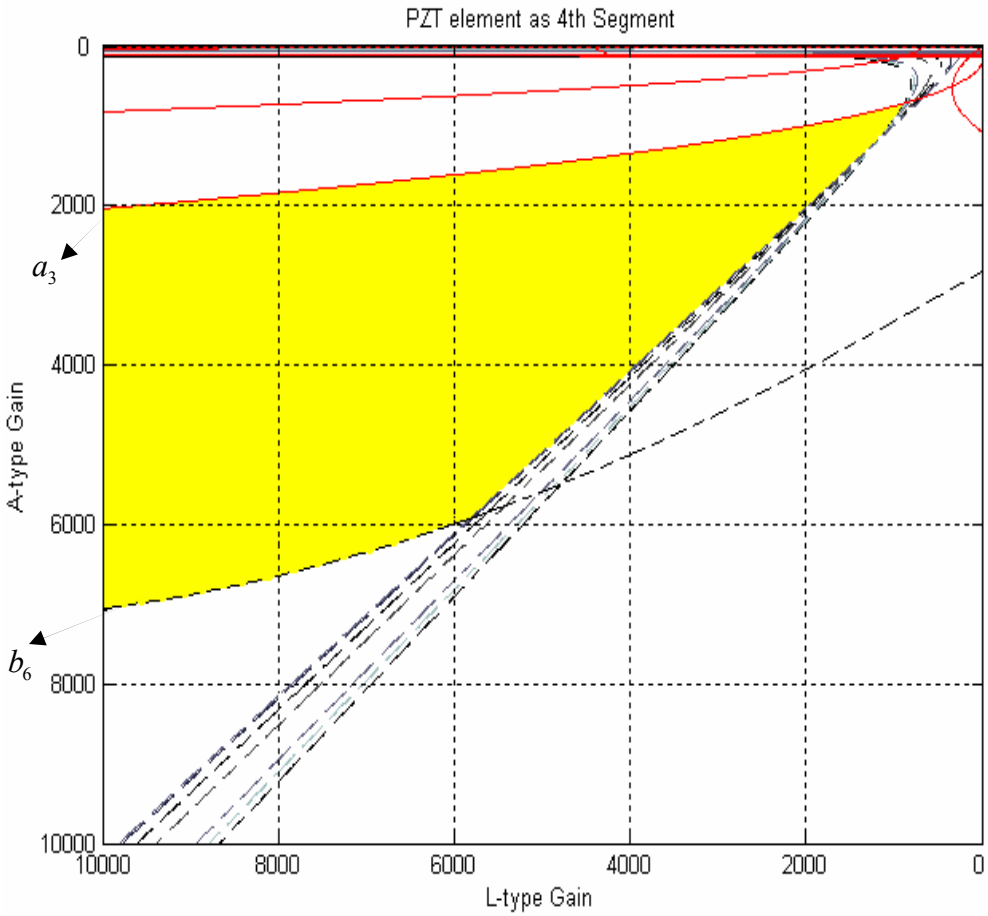

Figure 3.4. Feasible regions for the controller gains-PZT element as 4th Segment

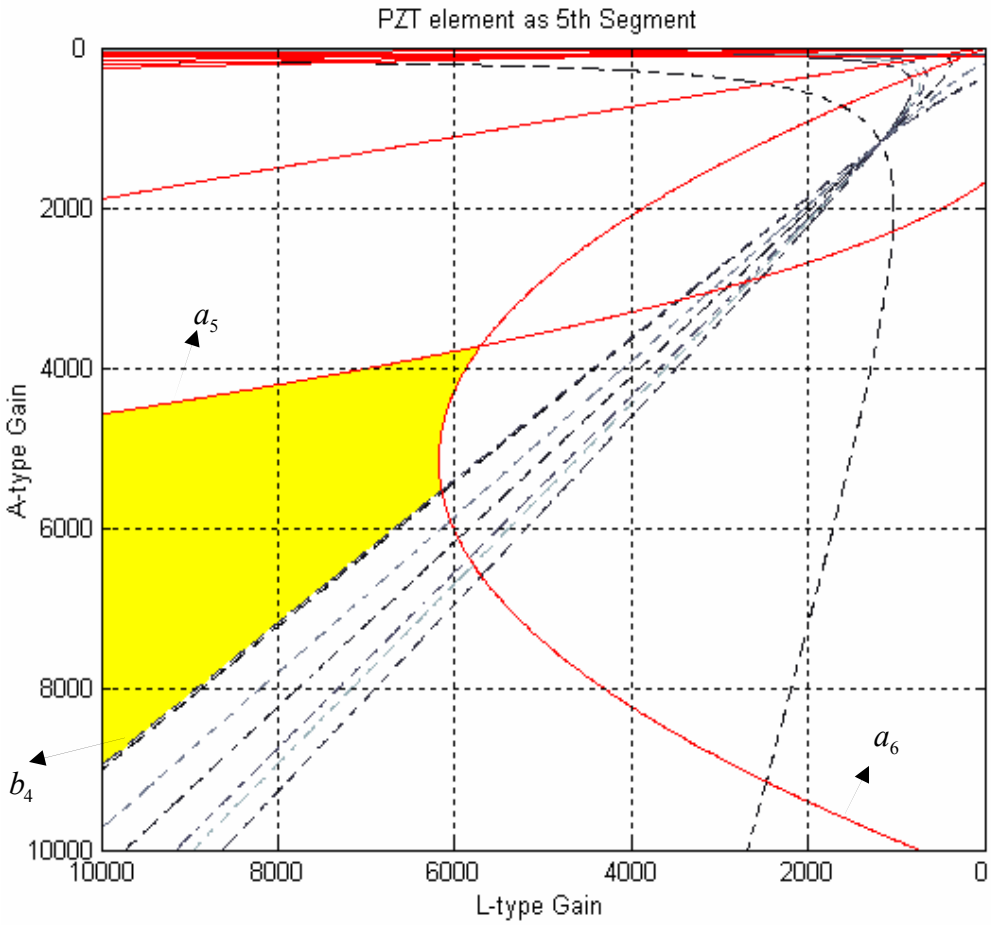

Figure 3.5. Feasible regions for the controller gains-PZT element as 5th Segment

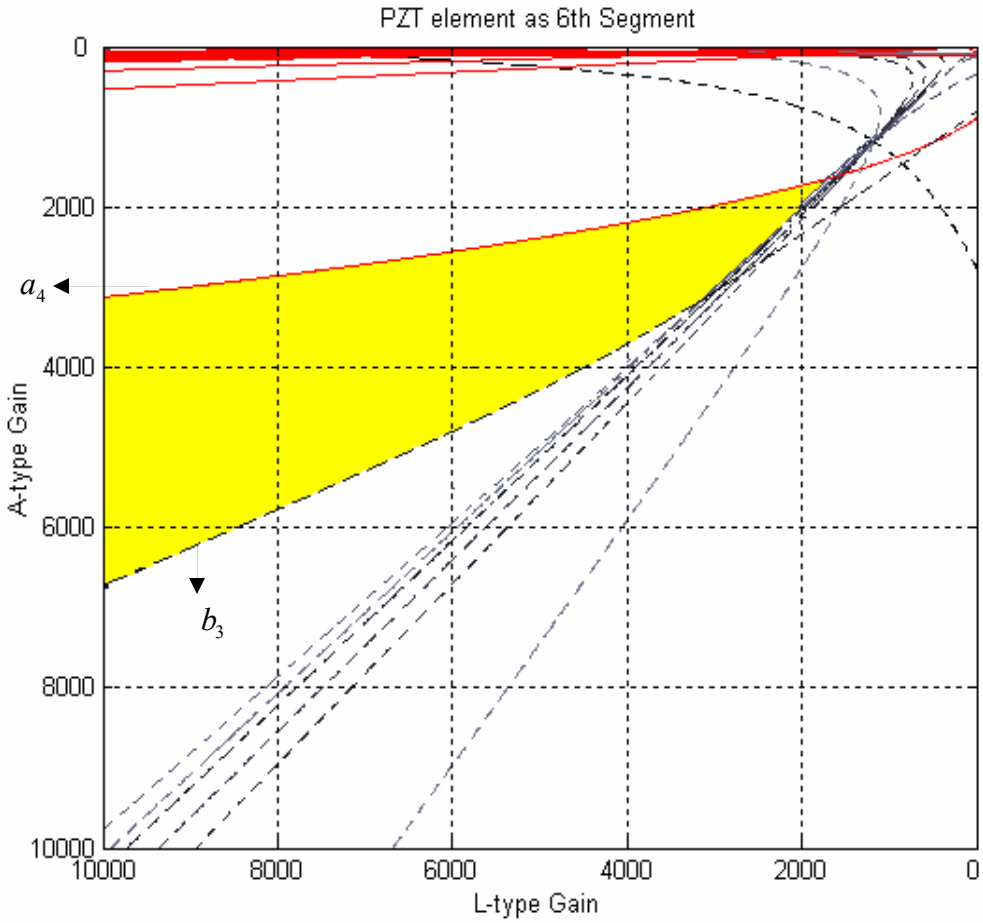

Figure 3.6. Feasible regions for the controller gains-PZT element as 6th Segment

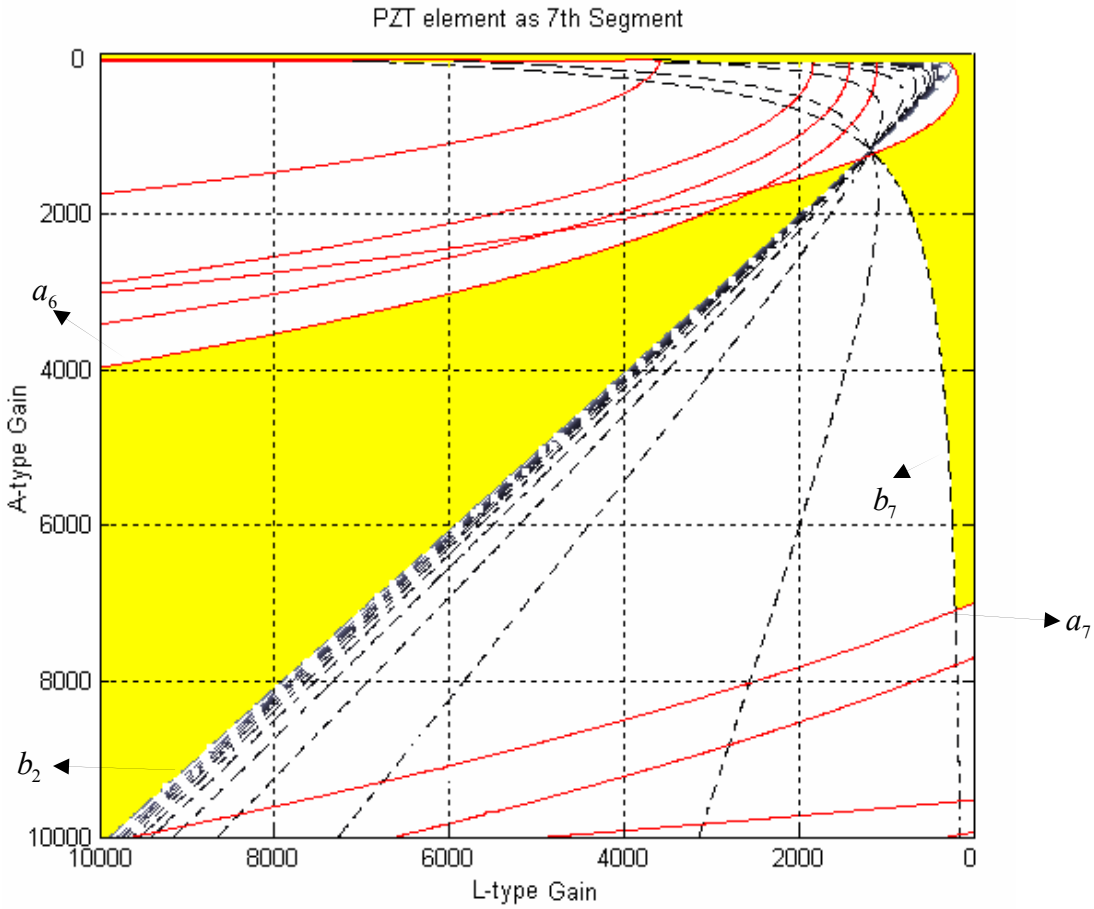

Figure 3.7. Feasible regions for the controller gains-PZT element as 7th Segment

In Figures 3.2-3.7, the solid-line curves indicate the zero contours for the envelope ($a_k = 0$) of each mode, and the dashed-line curves indicate the boundary for the onset of chattering. Each family of contours forms a region of potential control gain pairings and the intersection of these regions is the feasible region and is shown in light gray. In general, the stability criterion forms the lower bound on the gain values while the chattering consideration provides the upper bound. After defining the feasible regions for each possible placement point, the a_1, a_2 and a_3 contours were charted for each

placement point and these plots were used to select the placement and gains for the three PZT patches.

Within these light gray regions, the decay rate is generally largest near the most restrictive $b_k = 0$ contour. For example, Figure 3.8 shows a series of non-zero a_1 contours in the range $-81.12 \le a_1 \le -75.81$ in the case where the PZT patch is the second element in the assembled beam of Figure 3.1. Figure 3.8 shows that a PZT bonded at the 2nd segment effects the greatest damping of the fundamental mode when $k_L = 7500$ and $k_A = 7500$. There are three important observations drawn from Figure 3.8: very rapid improvement can be made in attenuating the first mode of vibration as k_A is increased; the a_1 contours are near horizontal and so for a chosen k_A gain there is very little improvement to be made by increasing k_L; and finally the beam of Figure 3.1 is unstable with the PZT patch in the second position if $k_A = 0$.

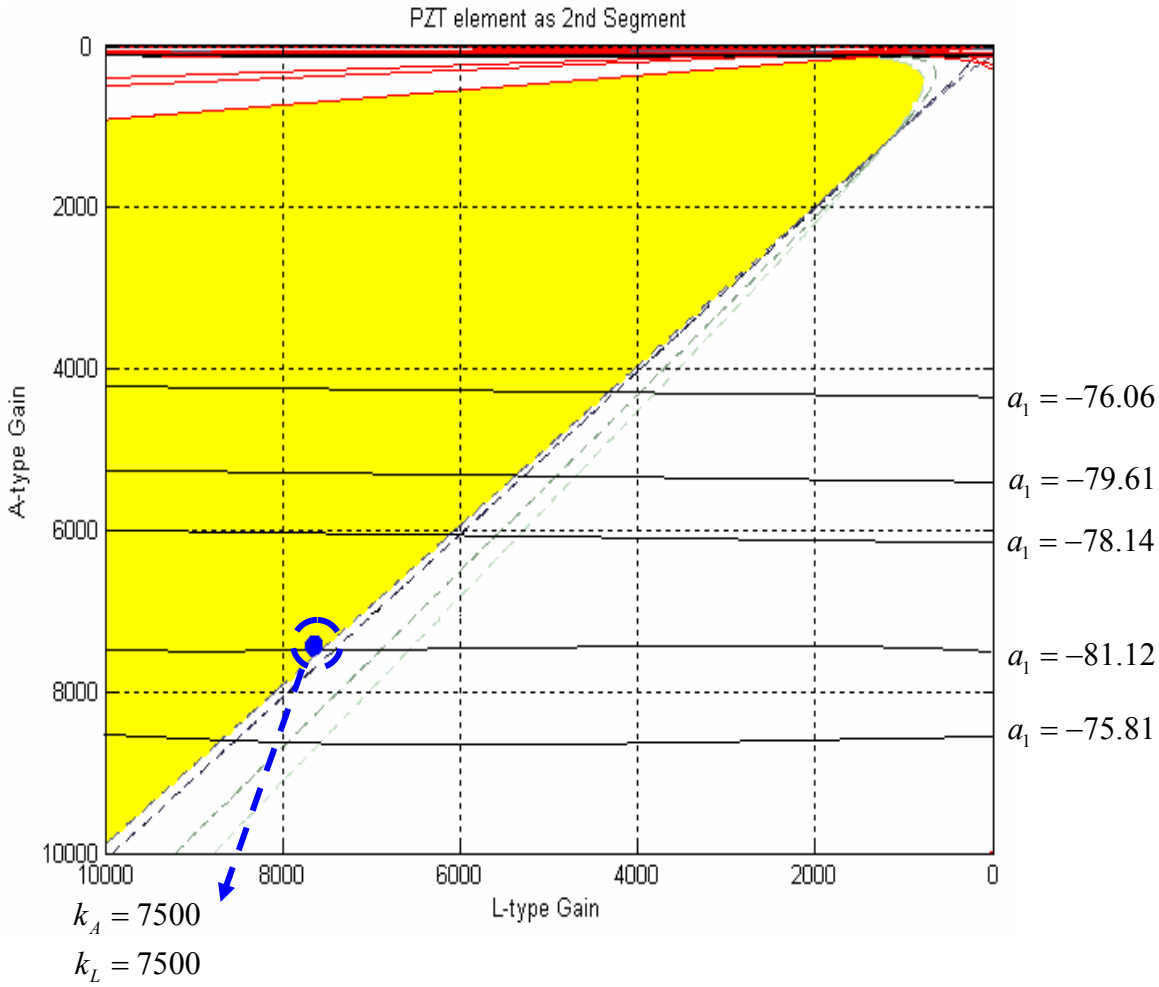

Figure 3.8. Contours of the decay rate for the first mode with the PZT patch in the second position.

Plots similar to Figure 3.8 were generated for $k = 1$ and $k = 2$ for all the possible placement points. The second mode of vibration was best suppressed when there was an actuator attached at the 4th segment with controller gains $k_A = 6000$ and $k_L = 6000$ while the most significant damping for the 3rd mode of vibration was seen when there was an actuator attached at the 6th segment with controller gains $k_A = 3000$ and $k_L = 3000$.

To compare to the proposed placements and PZT gains of [1], the use of L-type control alone on a PZT located at the tip of the flexible link was also examined. The

transient response of the flexible link when the PZT is at the tip, or seventh element, is summarized in Figure 3.9. In [1], a gain of $k_L = 7000$ is observed to provide the best damping of the first mode while maintaining stability. However, Figure 3.9 shows that the suppression of the 1st mode could have been vastly improved if angular type feedback had been employed with this particular choice of linear feedback gain.

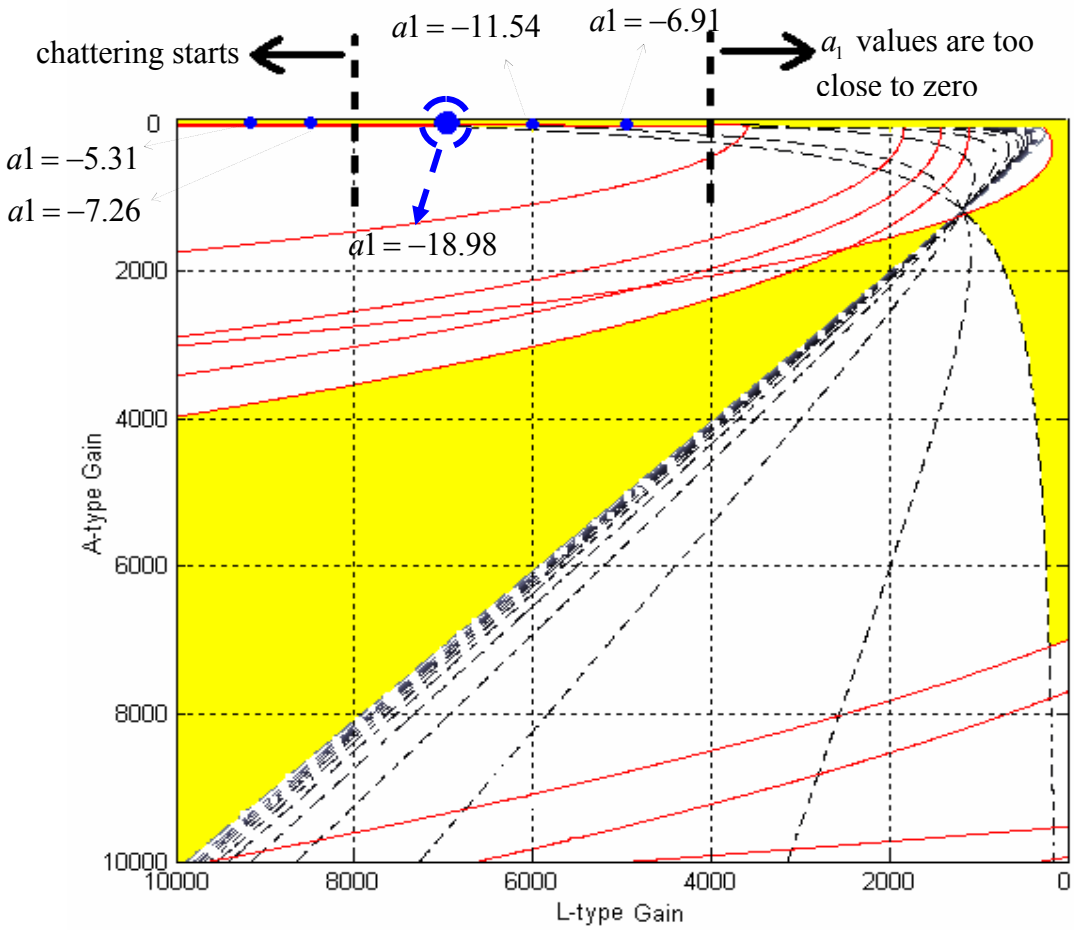

Figure 3.9. Investigation of the a_k values for L-type controller with the PZT patch in the seventh position.

Chapter 4 NUMERICAL SIMULATIONS

4.1 Chapter Overview

Simulations of slewing maneuvers of a single-link flexible manipulator were conducted using the proposed A-type, L-type, and composite controllers to compare the controller performances. In all these numerical simulation studies, the same hub controller was used to create the following slewing maneuver: rotating the flexible link from 0° to 30° over a 12 s period following the motion profile shown in Figure 4.1. In order to make a fair comparison of the three piezoelectric control methods, each controller was tuned so that the full potential of each method was realized. The tuning step was composed of the placement of the piezoelectric patches and the selection of the gains, k_A and k_L, for each controller as outlined in Chapter 3. Furthermore, one should keep in mind that, for the L-type controller setup, there is only one PZT present, which is located at the tip end and the gain value is named k_{Ltip} as indicated in Table 2.

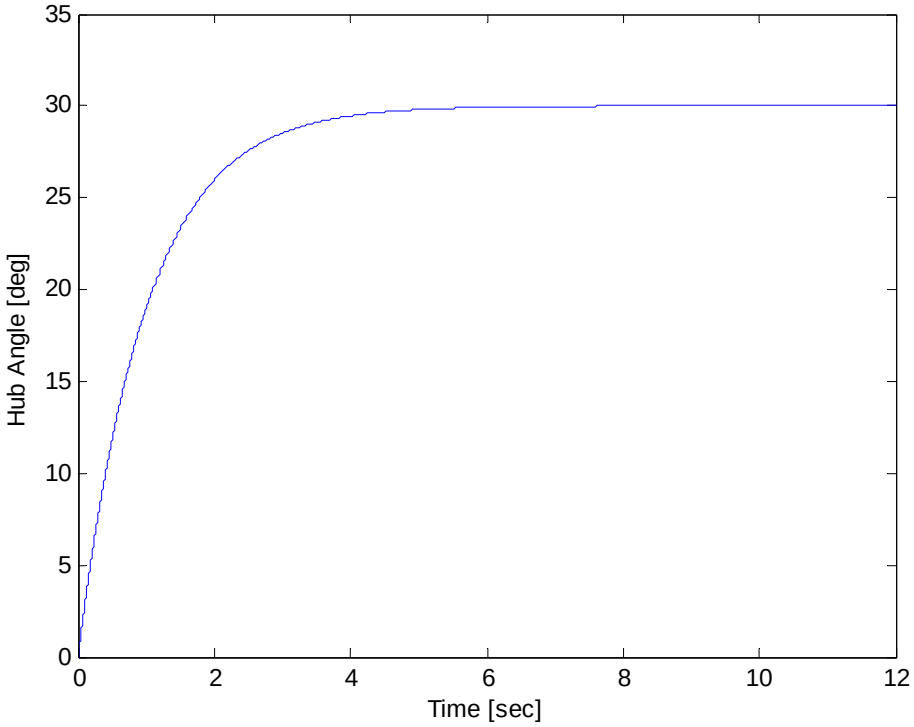

Figure 4.1 Hub rotation profile during the 12 seconds, 30 degree slewing maneuver.

4.2 Slewing Maneuver Description

Based on the results of §3.4, the surface bonded piezoelectric actuators were located as shown in Figure 4.2. The parameter values used to model the flexible link and the PZT actuators are given in the Table 1. In total, three PZT actuators were mounted on the link. The feedback gains for the hub controller were set as k_p = 1.39 (N-m/deg) and k_v = 0.87 (N-m-sec/deg). The feedback gains used for each control scheme and for each PZT actuator are shown in Table 2. For example, k_{L1} and k_{A1} are the gains of the L-type and A-type controller, respectively, for the PZT mounted at the root of the link. All these gains are set based on the tuning strategy of §3.4 and with respect to the physical limits of the actuators and the hub servomotor in terms of maximum applicable voltage and torque.

To avoid chattering while increasing the performance of the controllers, the gains are set using the feasible zones defined in Figures 3.2 through 3.7 for each PZT attached on the beam.

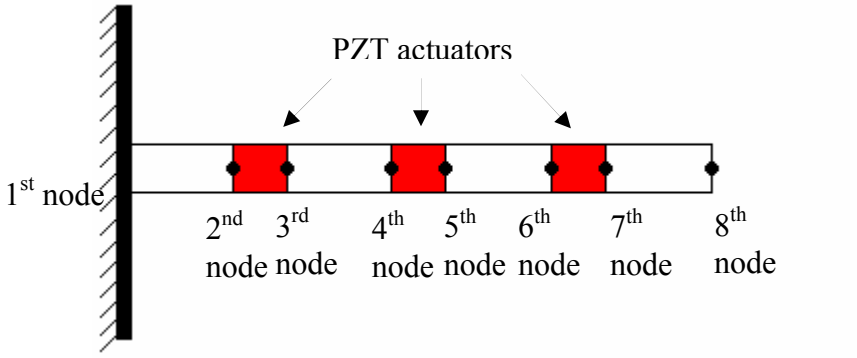

Figure 4.2 Final actuator setup on the assembled beam

Table 4.1
System parameters

	Beam	**PZT actuators**
Material	Stainless Steel	Lead Zirconium Titanate
Modulus	193×10^{9} N/m^2	63×10^{9} N/m^2
Length	1 m	0.05 m
Thickness	0.000381 m	0.000254 m
Width	0.03202 m	0.020574 m
Density	8000 kgm^{-3}	7600 kgm^{-3}
d_{31}	N/A	179×10^{-12} m/V

Table 4.2
Control gains and PZT Locations

Control Gains (V-sec/rad)	**L-Type**	**A-Type**	**Composite Controller**	**PZT Locations (from hub)**
k_{1tip}	7000	N/A	N/A	95 cm
k_{L1}	N/A	N/A	7500	21 cm
k_{L2}	N/A	N/A	6000	47 cm
k_{L3}	N/A	N/A	3000	73 cm
k_{A1}	N/A	7500	7500	21 cm
k_{A2}	N/A	6000	6000	47 cm
k_{A3}	N/A	3000	3000	73 cm

Table 4.3
Envelope and frequency values

When	**PZT at the 2nd Segment**			**PZT at the 4th Segment**			**PZT at the 6th Segment**		
Controller Type	L-Type	A-Type	Compo-site	L-Type	A-Type	Compo-site	L-Type	A-Type	Compo-site
a_1	-0.47	-64.04	-81.12	-0.31	-57.18	-70.33	-0.12	-48.93	-67.72
b_1	1.01i	2.17i	2.32i	1.12i	2.15i	2.28i	-0.99	2.09i	2.27i
a_2	-0.17	-2.37	-3.185	-0.19	-3.15	-5.46	-0.16	-1.02	-1.98
b_2	39.61i	47.36i	49.03i	39.8i	48.11i	50.47i	38.3i	45.8i	47.04i
a_3	0.002	-0.13	-0.214	-0.001	-0.12	-0.189	0.001	-1.02	-1.04
b_3	239.7i	291.96i	297.19i	244i	289.89i	291.5i	240i	299.62i	302.81i

4.3 L-Type Controller Simulation Results

Figure 4.3 represents the maneuver of the hub using the PD scheme in the absence of any PZT control strategy. As it was previously mentioned, the centrifugal stiffening and its affect on the vibration suppression can be seen in this figure. Also, Figure 4.3 helps

one to compare the PZT control affect in fair. After introducing the hub controller, Figure 4.4 shows the tip displacement during the simulation. The tip displacement reduction in the presence of the L-Type control is about 3% to 5%. Figure 4.5 shows the voltage applied to the PZT actuator during the maneuver, while Figure 4.6 indicates the force generated by the PZT as a response to the applied voltage. The force generated by the PZT is dependent on both material and geometric properties of the actuators as given in Eq. (4.1) [18]:

$$F(t) = (E_p d_{31} w_p) V(t) \tag{4.1}$$

where $V(t)$ is the applied voltage , d_{31} is the dielectric constant for the actuator, w_p is the width of the actuator and E_a denotes the Young's modulus of the piezoelectric actuator.

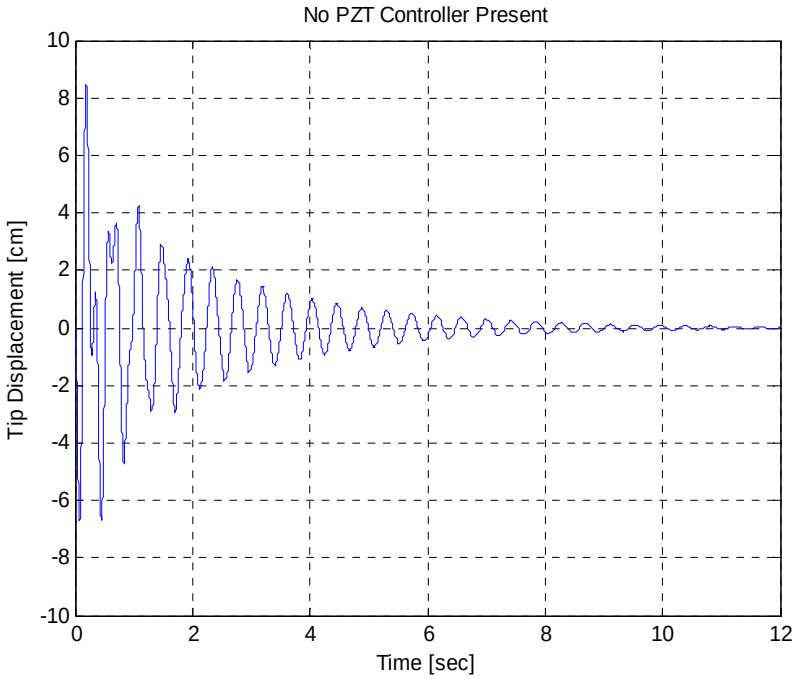

Figure 4.3 Closed-loop tip deflection responses using hub control only.

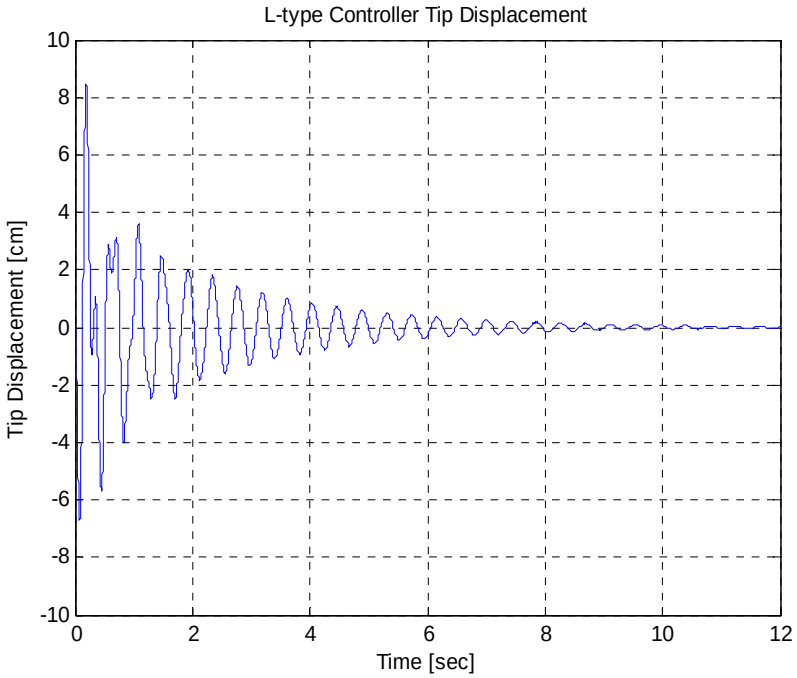

Figure 4.4 Closed-loop tip deflection response using L-type control.

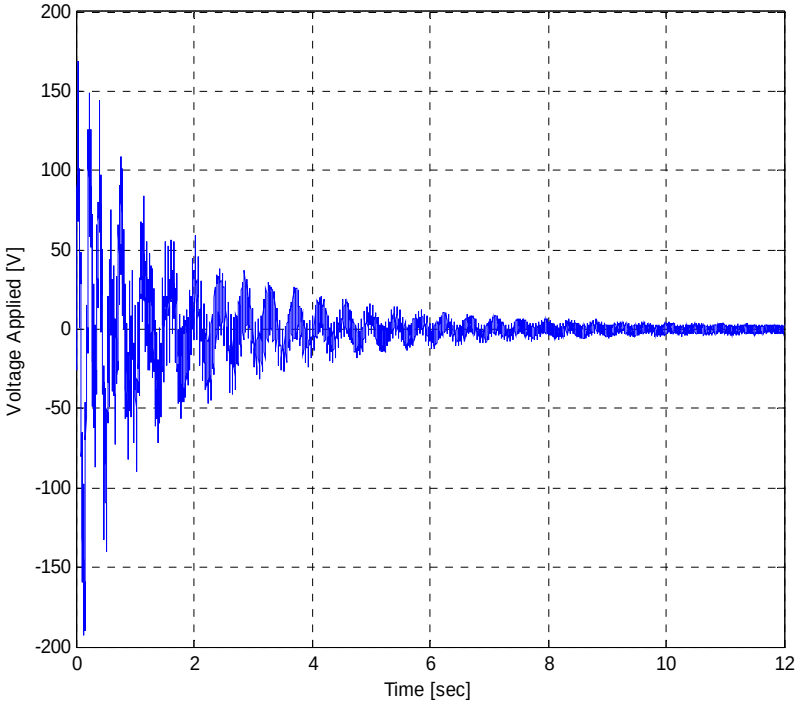

. ***Figure 4.5*** Control voltage applied to PZT at the tip by using the L-type controller

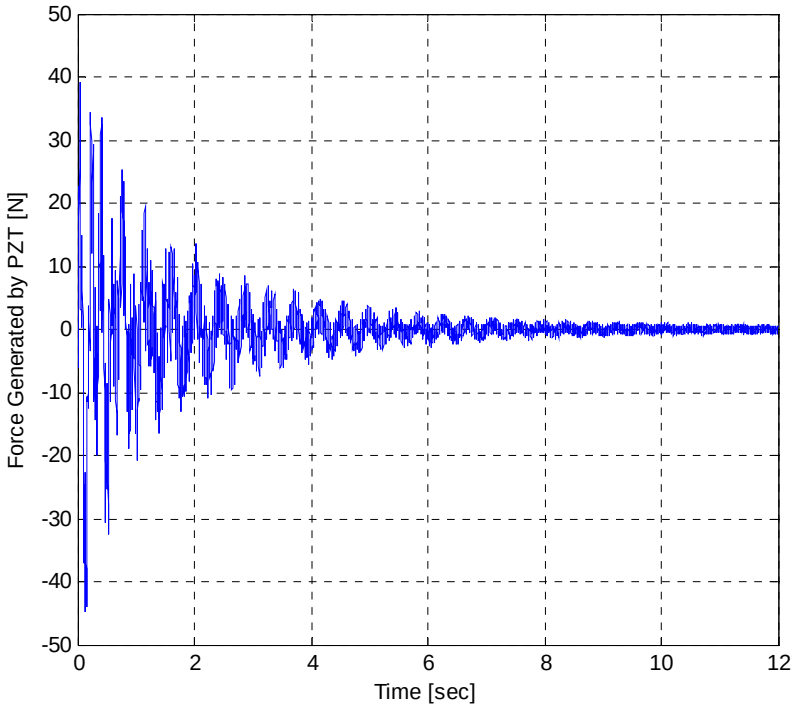

Figure 4.6 Force generated by the PZT at the tip using the L-type controller

4.4 A-Type Controller Simulation Results

The simulation results achieved with the A-Type controller are shown below. Figure 4.7 gives the tip displacement of the assembled beam under the A-Type control scheme. Figures 4.8 through 4.10 indicate the voltage applied to the PZTs where Figures 4.11 through 4.13 indicate the force generated by the actuators in the response to the control voltage applied.

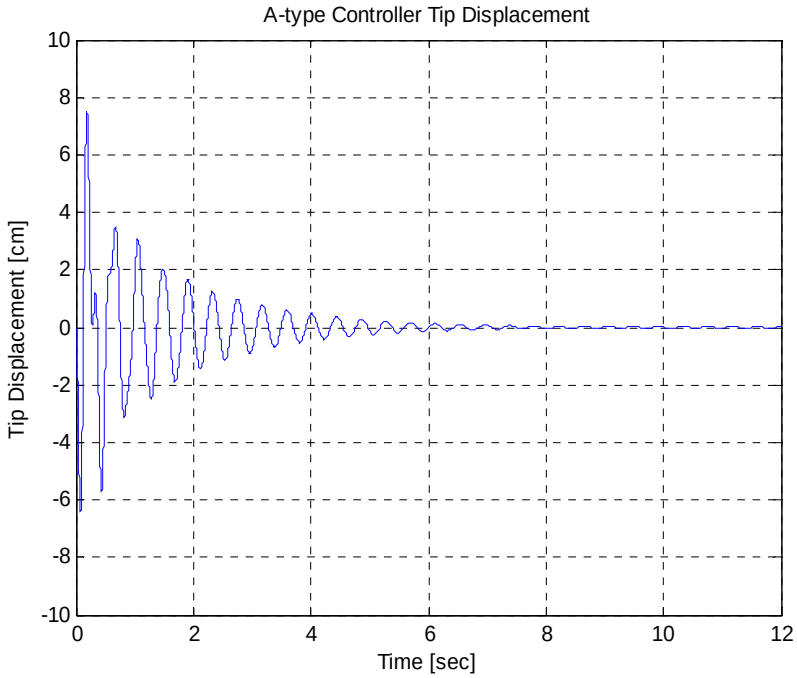

Figure 4.7 Closed-loop tip deflection response using A-type control.

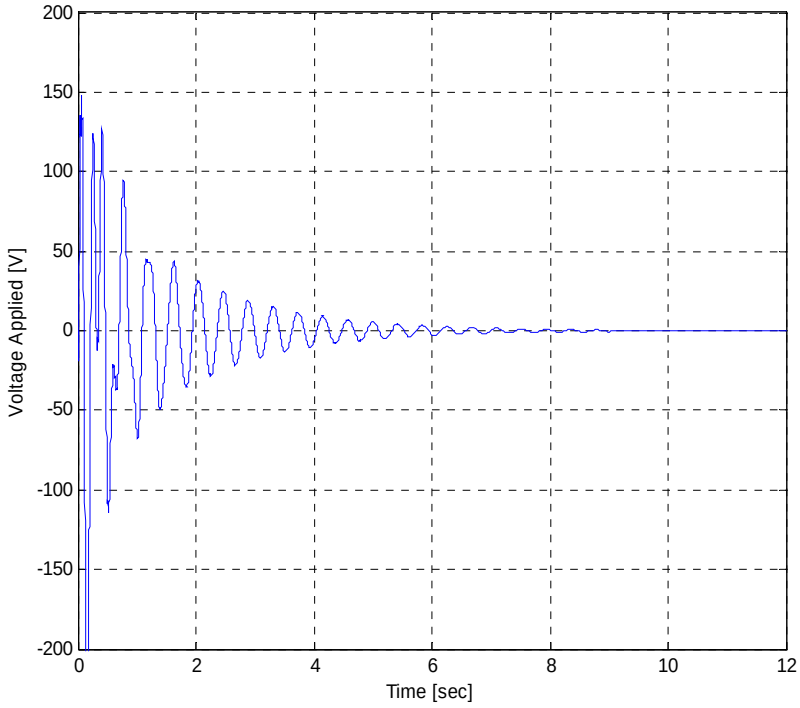

Figure 4.8 Control voltage applied to the 1st PZT by using the A-type controller

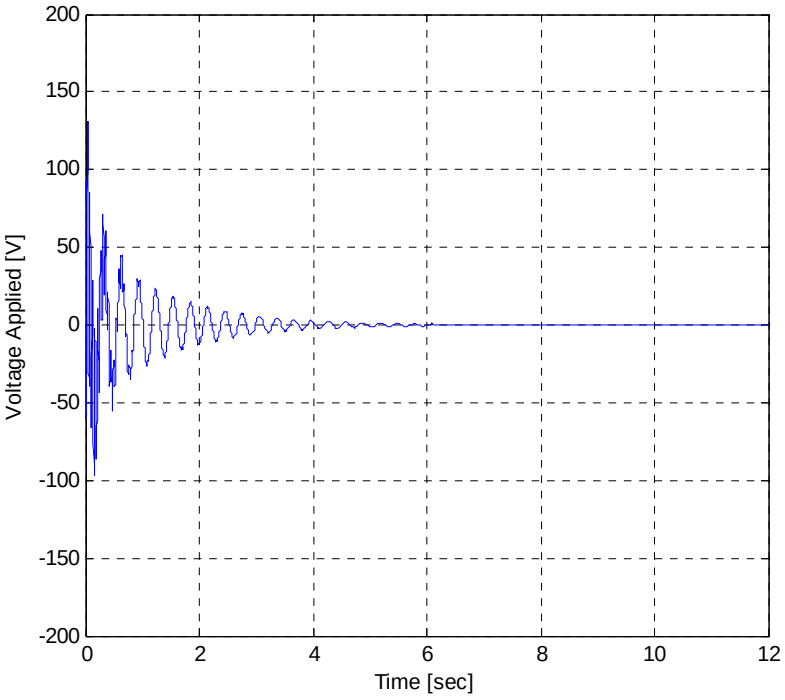

Figure 4.9 Control voltage applied to the 2nd PZT by using the A-type controller

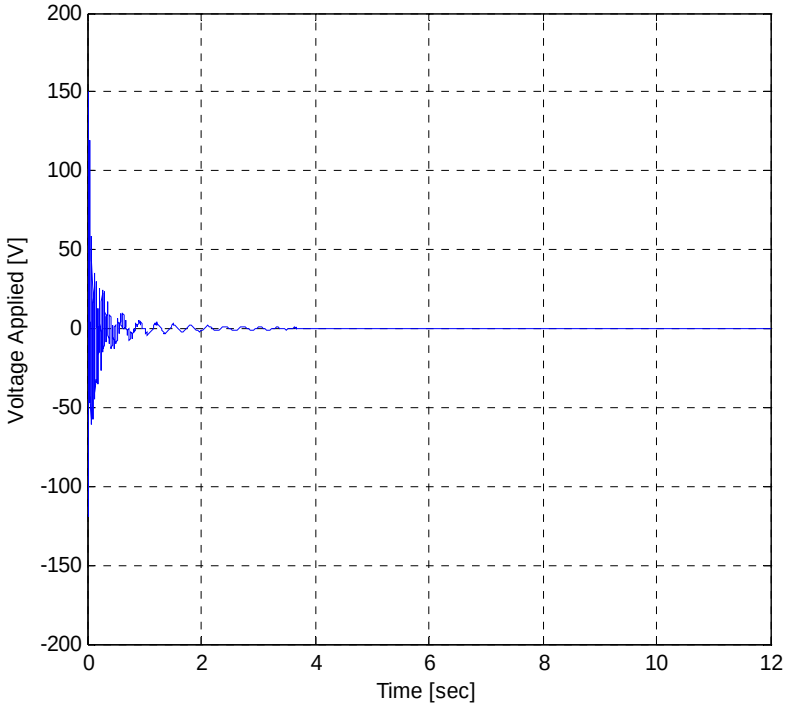

Figure 4.10 Control voltage applied to the 3rd PZT by using the A-type controller

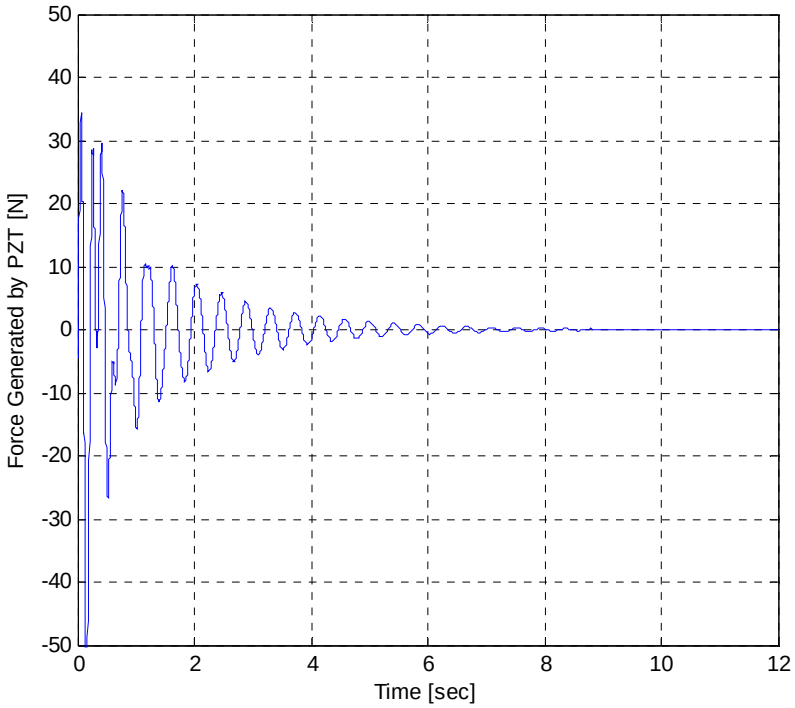

Figure 4.11 Force generated by the 1st PZT using the A-type controller

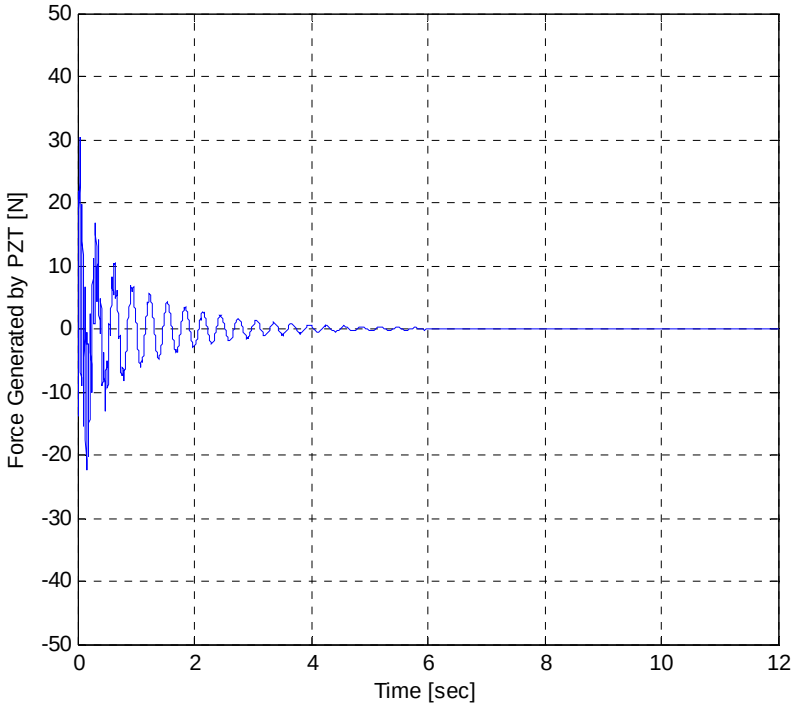

Figure 4.12 Force generated by the 2nd PZT using the A-type controller

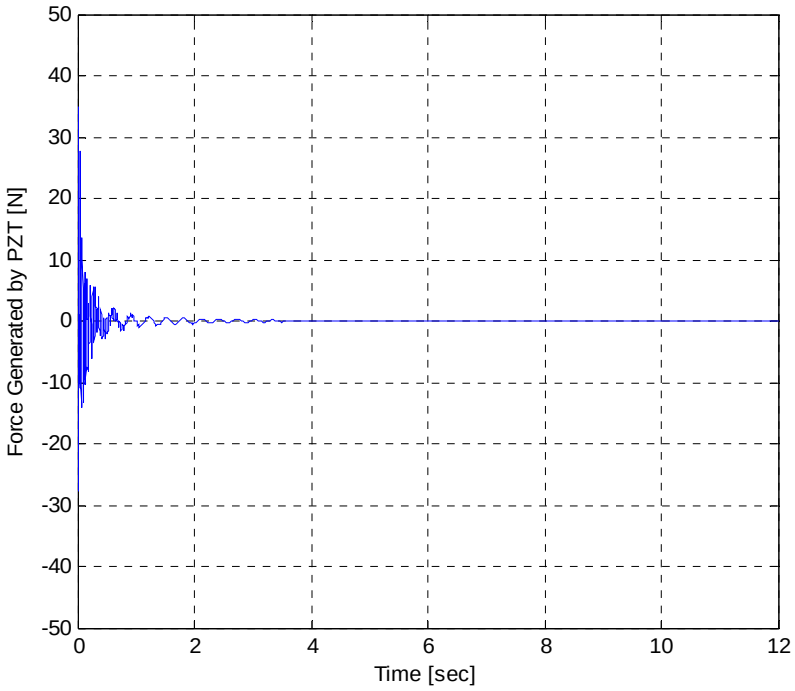

Figure 4.13 Force generated by the 3rd PZT using the A-type controller

4.5 Composite Controller Simulation Results

Similarly, Figure 4.14 represents the tip displacement of the assembled beam under the Composite control scheme. Figures 4.15 through 4.17 indicate the voltage applied to the PZTs where Figures 4.18 through 4.20 indicate the force generated by the actuators in the response to the control voltage applied.

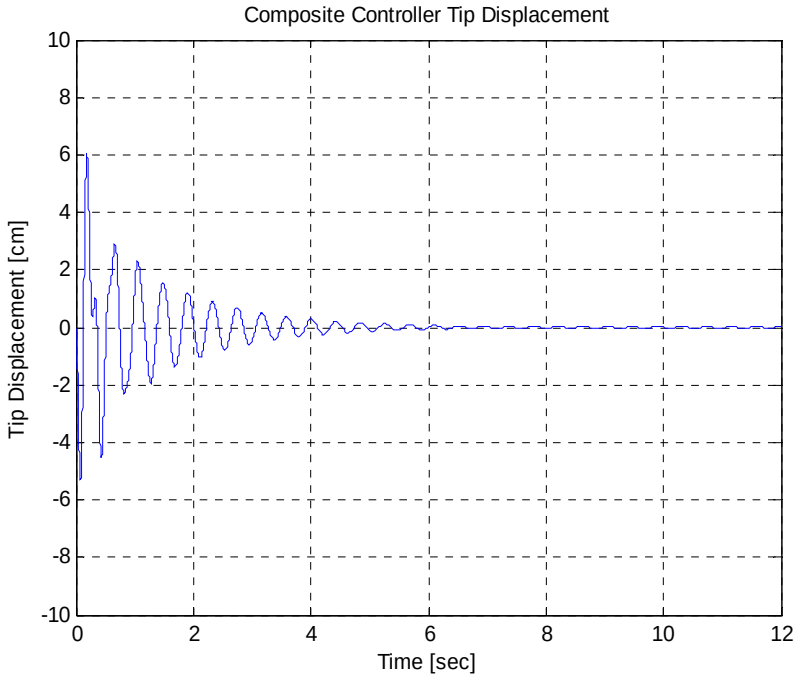

Figure 4.14 Closed-loop tip deflection response using composite control.

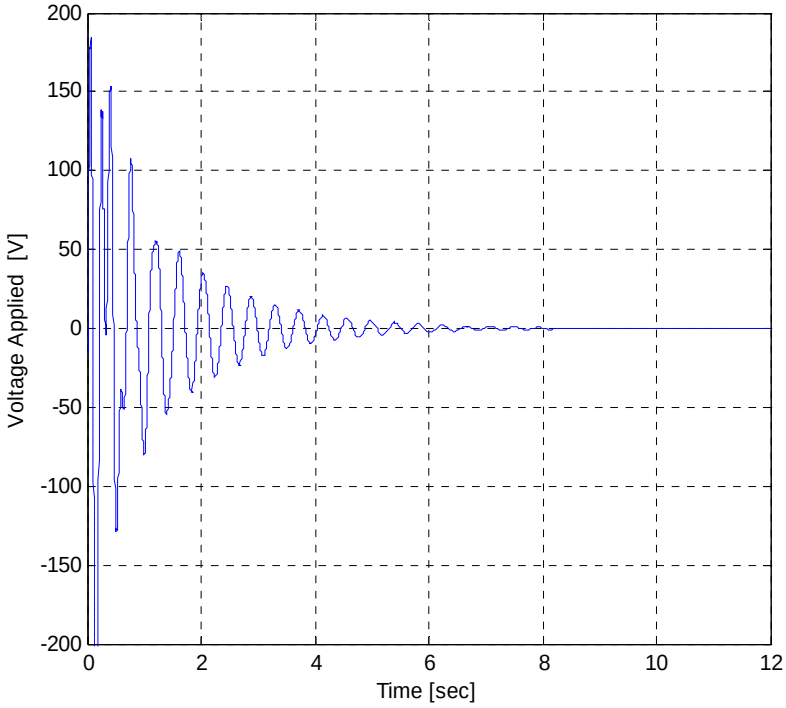

Figure 4.15 Control voltage applied to the 1st PZT by using the Composite controller

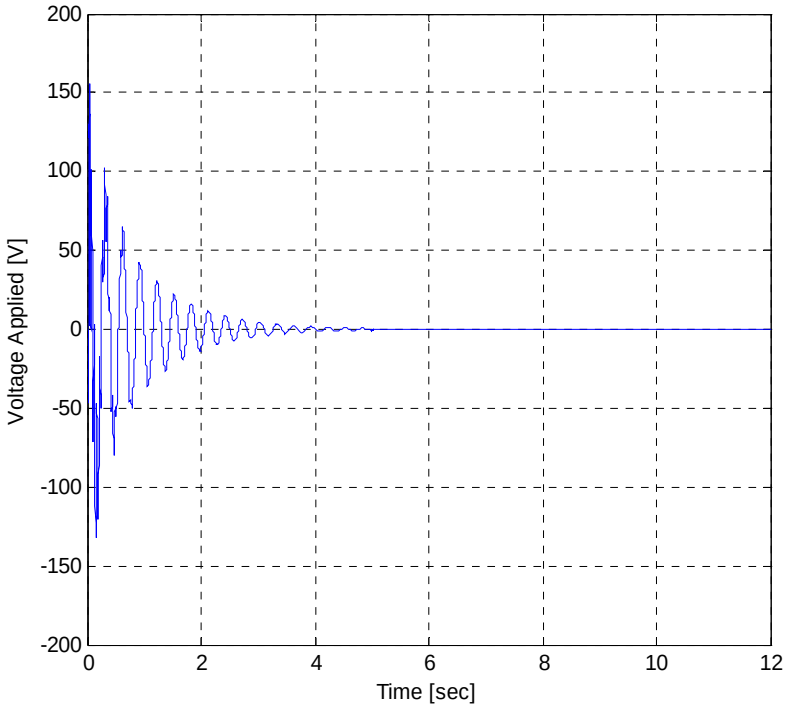

Figure 4.16 Control voltage applied to the 2nd PZT by using the Composite controller

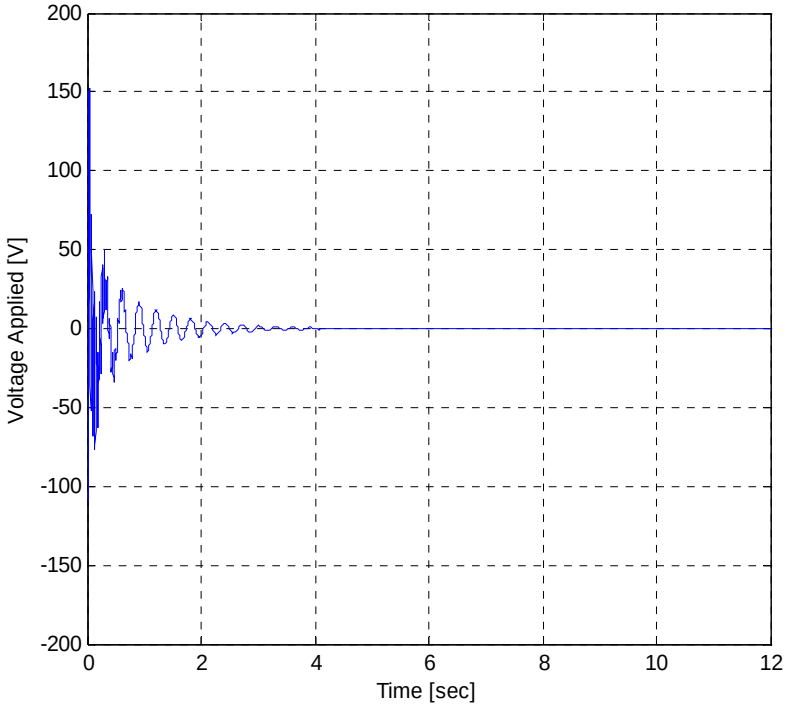

Figure 4.17 Control voltage applied to the 3rd PZT by using the Composite controller

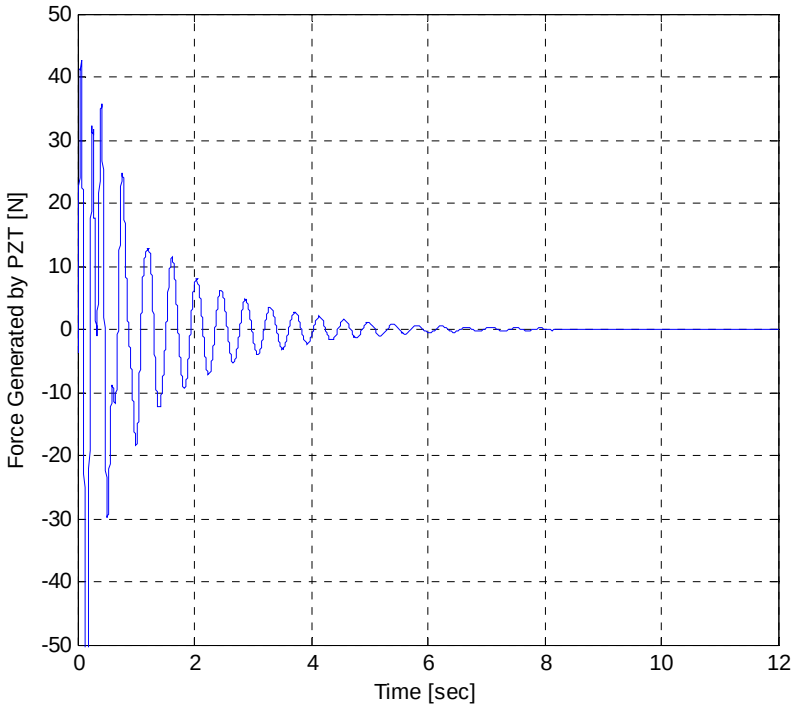

Figure 4.18 Force generated by the 1st PZT using the Composite controller

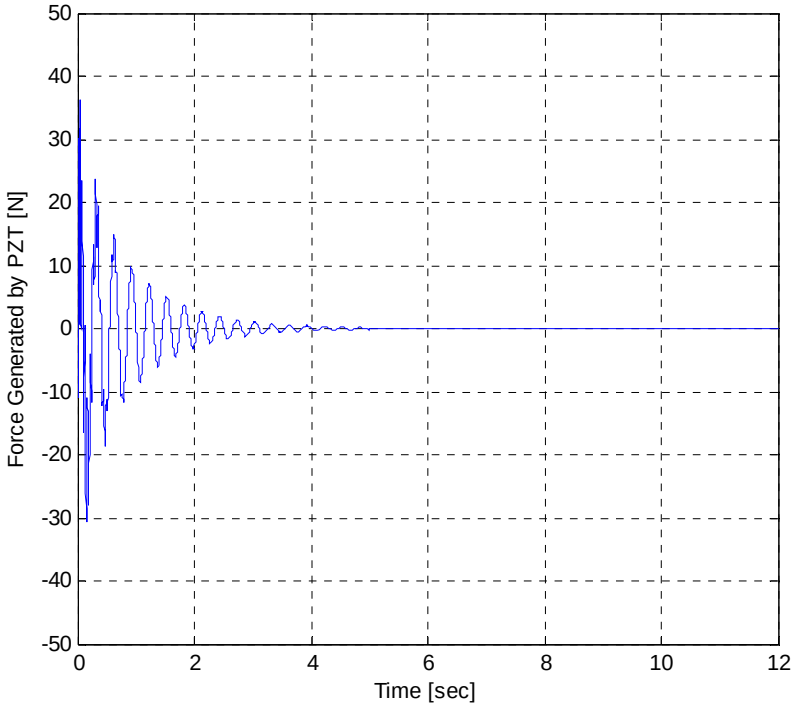

Figure 4.19 Force generated by the 2nd PZT using the Composite controller

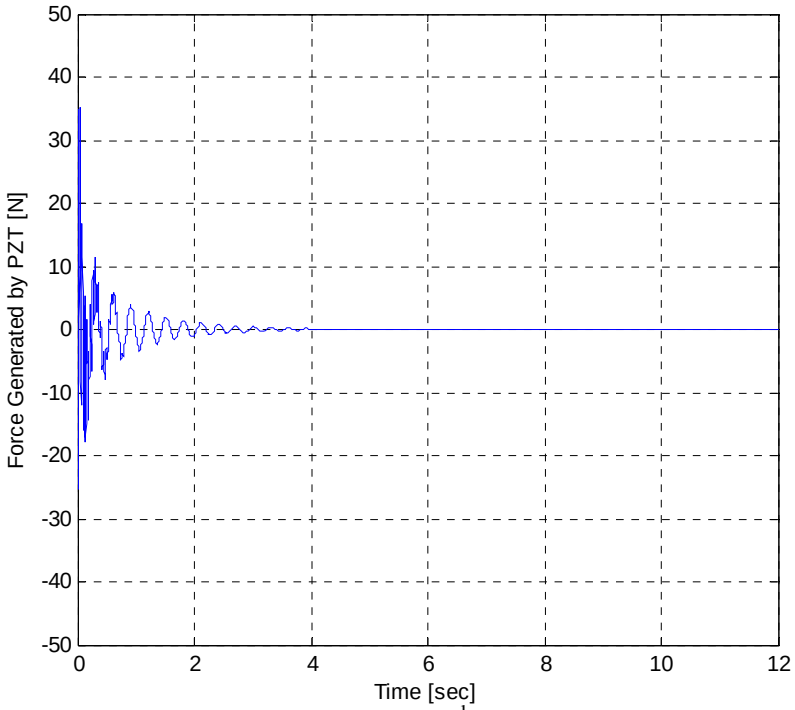

Figure 4.20 Force generated by the 3rd PZT using the Composite controller

4.6 Discussion of Simulation Results

Figures 4.3, 4.4, 4.7 and 4.14 show the elastic tip deflections for the proposed controllers. It can be seen that superior vibration suppression is achieved using hub control in partnership with the composite piezoelectric control scheme. In general, the A-type controller performs better than the L-type controller, as can be seen by comparing Figures 4.4 and 4.7. The use of the composite controller results in even faster vibration suppression (Figure 4.14). To clarify the benefits of the composite method, Figure 4.21 shows the elastic tip deflections of all the various approaches.

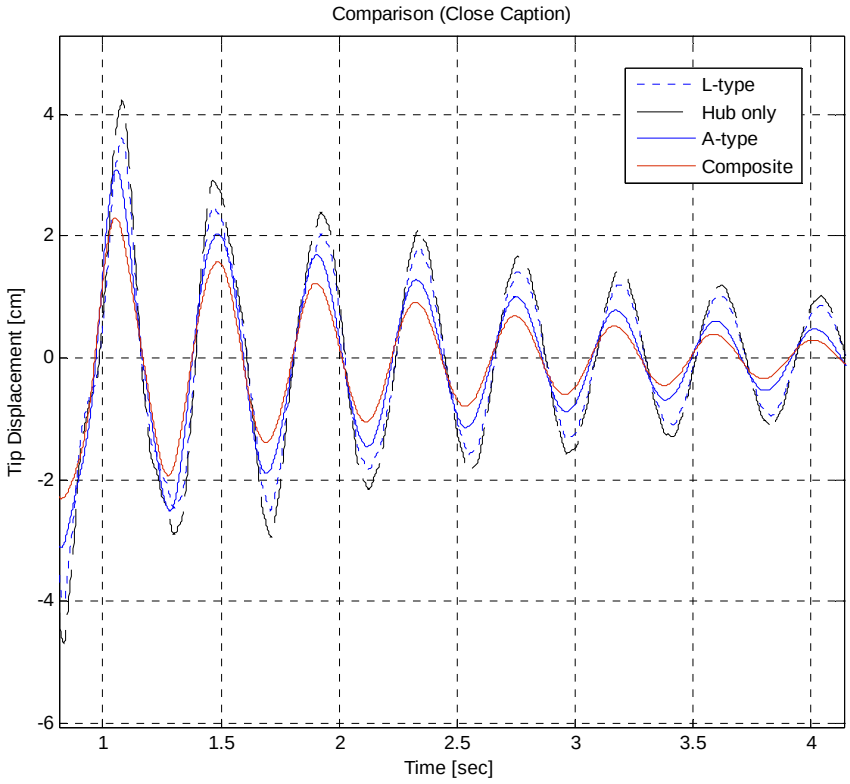

Figure 4.21 Closed-loop tip deflection responses comparison.

Figures 4.5, 4.8-4.10 and 4.15-4.17 illustrate the control voltages applied to the PZT actuators during the simulation by using the L-type, the A-type and the composite controllers respectively. As can be seen in Figure 4.5, since the control voltage applied is proportional to the linear velocity difference at the edges of the actuator, using the L-type control strategy is more energy intensive. Power consumption wise, the A-type and the Composite controllers are much more economic.

The forces generated by using the L-type, the A-type and the Composite controllers can be seen as in Figures 4.6, 4.11-4.13 and 4.18-4.20, respectively. The force profile that PZT actuators produce is similar to the voltage profile applied on the PZTs since there is

a linear relation between the voltage and the developed force. Therefore, similar comments can be made on those figures as for the ones regarding to the applied voltage.

Chapter 5 EXPERIMENTAL RESULTS

5.1 Chapter Overview

In this section, a detailed overview of the experimental testbed is given. The flexible manipulator, shown in Figure 5.1, was built to verify the proposed methodology of using ShapeTape^{TM} to provide the linear and angular velocity feedback that is necessary to implement the composite PZT control strategy. The rotatory hub was used to excite the vibration on the flexible structure by executing a slewing maneuver as outlined in §4.1. The PZT actuators were bonded at the locations given in §4.2, and all the material properties and the gain selections were as indicated in §4.2 - Tables 4.1 and 4.2. The experiments provided validation of the theoretical placement and gain selection process.

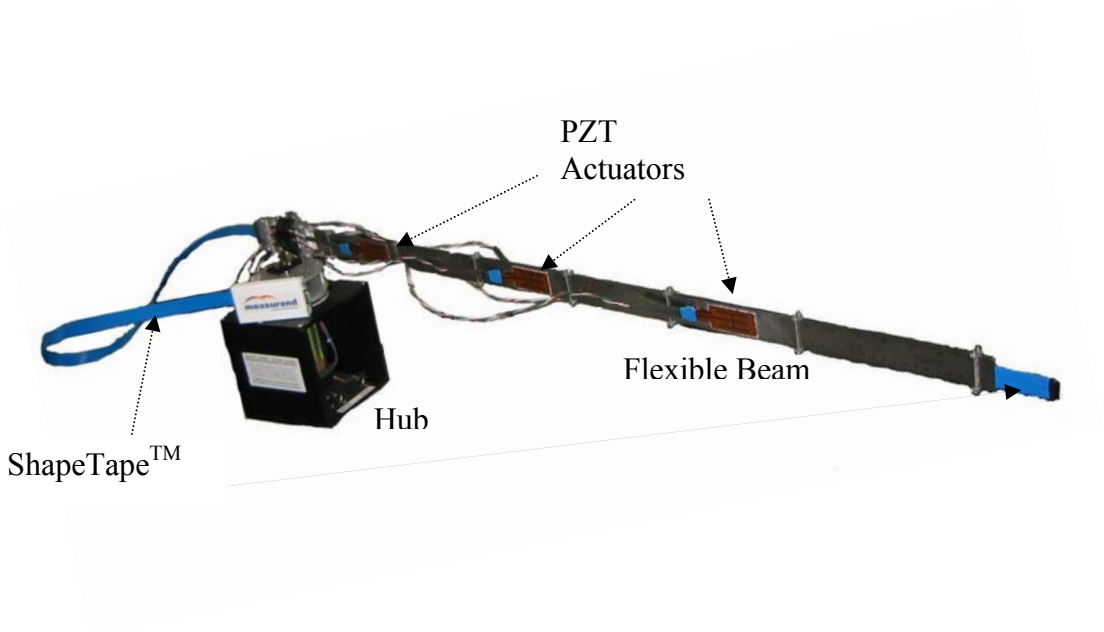

Figure 5.1. Assembled beam and the equipments used in the test setup

5.2 Hardware Description

A schematic diagram of the overall system is given in Figure 5.2. The assembled beam is attached to a hub, which is rotated by a Pittman-S14204 DC (brushed) servo motor. The torque constant k_t and the rotor inertia J_m are 32.7×10^{-3} N·m/A and 2.61×10^{-5} kg·m^2, respectively. The motor electric constant τ_E and the motor's viscous damping (zero source impedance) K_D are 1.58 ms and 1.28×10^{-5} Nm/(rad/s) respectively. The hub rotation is monitored by a US Digital-E3 encoder which has a resolution of 0.036°. The motor is driven by a Quanser UPM-2405 power module which can generate 120 VAC. This hub is interfaced to a host computer by using a Quanser-Q8 (8-channel) PCI-express terminal board. As shown in Figure 1, the flexible beam is comprised of two Gaebel SS-339 series stainless steel rulers. The rulers are held in parallel using custom

machined fixtures that are regularly spaced along the length of the assembled rulers. A Measurand ShapeTape™ fiber-optic sensor array, discussed in detail in Appendix B, is held between the parallel flat faces of the steel rulers. While the tape is in contact with the inner faces of both rulers, there is very little pressure on the tape itself due to the custom fixtures which ensure that the gap between the rulers matches the width of the tape itself. Pressure on the sensing fibers increases the noise on the ShapeTape™ signal, thus should be avoided. Furthermore, the data transfer between the host computer and the ShapeTape™ is provided a DAQ unit which is a multiplexer that converts throughput intensity signals from each fibre-optic sensor into a digital output that contains the 16 curvature values over the length of each sensing region. Additionally, 6 Mide QP-20n piezoelectric strain actuators are bonded in pairs to the outer surfaces of the stainless steel rulers to facilitate implementation of the L-type, A-type and composite control laws given in Eqs. (2.45), (2.43) and (2.47) respectively. In order to drive the actuators, a 10 channel Sensortech SS-10 high voltage power amplifier is used. This amplifier is interfaced to a host computer through the Quanser Q8 board. The amplifier can generate up to ±270 V, but is limited to ±200 V to prevent breakdown of the Mide PZT actuators.

The servo motor is driven by the PD control scheme of Eq. (2.39). A slew of 30˚ is attempted in 22 seconds (limited by the weak torque capacity of the Pittman servo motor) and this maneuver is sufficient to induce significant vibration in the beam. The sensor array, ShapeTape™, captures the motion of the beam and feeds back the shape deformation in terms of nodal angular and linear displacements. The main command and communication module, which directs all control experiments, is implemented in Matlab and compiled by a program called WinCon (from Quanser), which can manipulate the

Matlab Real Time Workshop (RTW) and the Quanser-Q8 board. The linear and angular velocity signals at the ShapeTape™ sensing locations are calculated using a least squares FIR differentiator, and these velocity signals are smoothed using a linear Butterworth filter with a cut-off frequency of 30 Hz. This corner frequency was chosen in order to capture the first 3 modes of vibration and to avoid the noise mentioned earlier. As soon as the ShapeTape™ velocity data is acquired and filtered, the WinCon software drives the high voltage power amplifier via the QUANSER-Q8 board to actuate the PZTs according to the proposed control laws. The actuation signal between the Q8 board and the Sensortech amplifier is an analog output of ±6 V.

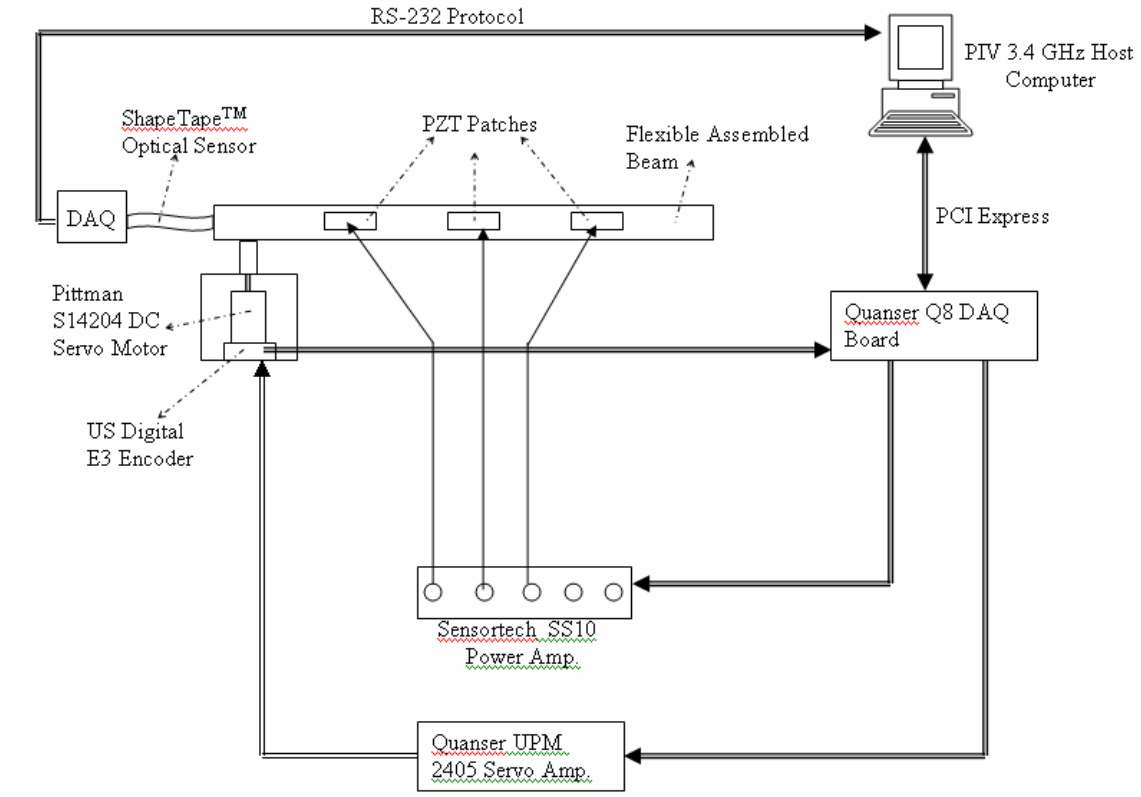

Figure 5.2. Schematic diagram of the experimental test setup

A significant difficulty in the hardware layout of Figure 5.2 is the synchronization of the two different communication units. The Quanser-Q8 board interfaced with the host computer via a PCI express connection and the Measurand DAQ unit interfaced via an RS-232 serial connection. As the control instructions are executed by the Q8 board, it was used as the master controller. To synchronize the ShapeTape™ feedback, hub control and piezoelectric control signals, a half-duplex communication between these two units was used. According to the half duplex protocol, data transmitted by the Measurand ShapeTape™ is acquired as determined by the master controller running on the Q8 board. However, this solution leads to a delay between the generation of the ShapeTape™ signal and its acquisition by the Quanser-Q8 board. However, using the RTX software that is embedded in WinCon, this delay can be made minimal.

As mentioned earlier, two Gaebel SS-10 rulers comprise the flexible link and collectively have the physical properties similar to those indicated in Tables 4.1 and 4.2. The assembly of the rulers is shown in Figure 5.3. Using custom machined fixtures mounted at regular intervals along the ruler assembly, the ShapeTape™ is held between the parallel faces of the steel rulers. The ShapeTape™, is positioned to sense the elastic displacements and velocities at the edges of the 7 different sensing zones outlined in §3.4.

The PZT patches are bonded on to outer surface of the rulers as the active dampers. To prevent additional unaccounted damping, all the PZT cables were routed in a slack manner such that they were never tensioned during a maneuver. A sampling frequency and control update rate of 100 Hz was used in all experiments. The choice of 100 Hz is determined due to the bandwidth limitations of the ShapeTape™ fiber optic sensor array

which can only reach up to 120 Hz refresh rate. However, this bandwidth is still good enough to capture the first few modes of the link vibration.

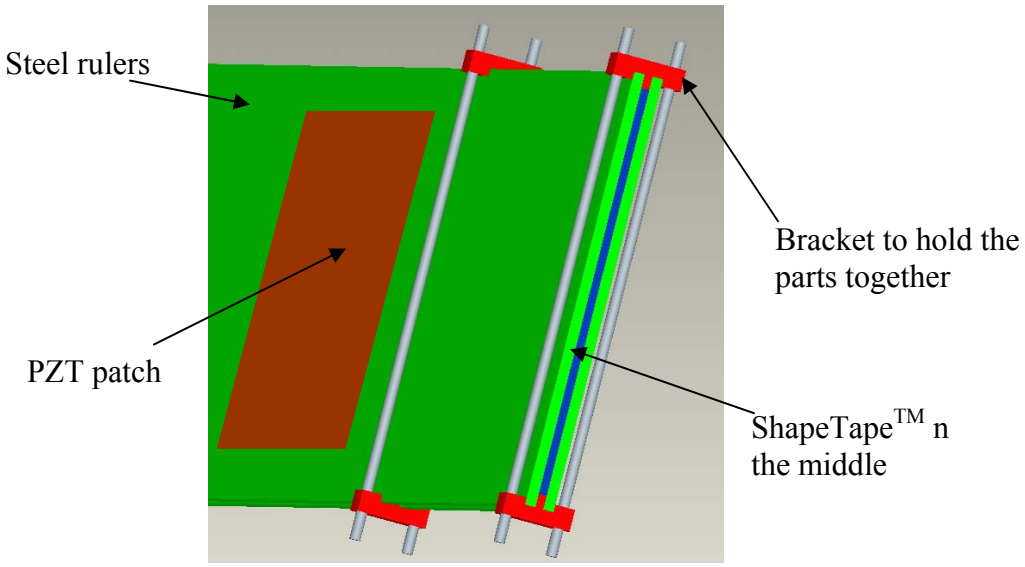

Figure 5.3. Illustration of composite beam/link assembly

5.3 Experimental Results and Discussion

The assembled flexible beam, was driven through controlled slewing maneuvers of 30º to verify the effectiveness of the three piezoelectric control strategies outlined in §2.6. In the analysis of the experimental results, the tip displacement was used as the performance metric. The deflections of the beam tip achieved using the various control schemes are shown in Figures 5.4 and 5.5. As seen in these figures, a vibration of up to 20 cm (peak-to-peak), or 20% of the link length, is experienced when only the hub controller is present. Using only hub control, the vibration was observed to die out after 22 seconds. In the presence of the active vibration control strategies, the vibration induced by the maneuver was suppressed faster than the hub controller itself. Indeed, the

reduction in vibration amplitudes in the presence of the A-type and the Composite controllers were about 30% and 45% respectively as seen in the Figure 5.4. The composite controller exhibits the best performance in damping out the vibration as seen in Figure 5.4, which is plotted on top of the hub controller response for comparison purposes. Figure 5.4 clearly demonstrates the efficacy of the proposed composite controller: large amplitude elastic vibrations are dramatically reduced by the action of the composite controller.

Figure 5.5, exhibits the response that occurs when only the L-type controller is used. However, as discussed in §2.5.3 and §3.4, the use of L-type control at interior points in the beam can lead to instabilities when the hub is inactive. In the experiment discussed here, the three piezoelectric elements were driven by the L-type controller and the hub controller. The additional the hub controller activity acts to stabilize the beam. However, the tip deflection is observed to demonstrate a persistent vibration long after one expects the vibration to dissipate. Figure 5.5 shows that the L-type method is costly in terms of both time and power consumed.

Figure 5.6 and 5.7 show the effects of changing the piezoelectric gains. All of the gain parameters were increased by 15% for each of the three PZT actuators. The differences in the tip deflection seen between the cases of Figures 5.6 and 5.7 is proof of the gain selection process - consistent with the observations in §3.4, increasing the piezoelectric gains does not necessarily improve the control response. Since the gain increase applied was not drastic, the same overall behavior is followed in Figures.5.6 and 5.7.

In all of the cases considered except the L-type, an immediate impact on the vibration response can be seen at the very beginning of the maneuver due to the hub controller. After this initial attenuation, the PZT controllers further suppress the oscillations of the flexible link.

During the experimentation, a 4 to 6 cm DC offset is seen on the vibration response. There are a couple of reasons for this offset. Firstly, the ShapeTape^{TM} claims up to 3% of inaccuracy in measuring tip deflections which translates to about 3cm of measurement error for the 1 m long flexible link. Secondly, in order to avoid applying pressure on the sensor, the custom fixtures were used to ensure the separation of the ruler faces. However, the fixtures did not grip the rulers perfectly and during a slewing maneuver the rulers would slide at different amounts through each fixture, inducing a curvature at that fixture location. These curvatures would remain if the stiction between the fixtures and the rulers prevented the rulers from retaining their initial positions. This residual curvature at the fixture locations produced noticeable residual tip deflections, as shown in Figure 5.8. Furthermore, it was observed that the rulers have natural curvature and are not truly flat. As the amplitude of the vibration grows, the tendency to create a static deformation (the DC offset) was observed to increase as well..

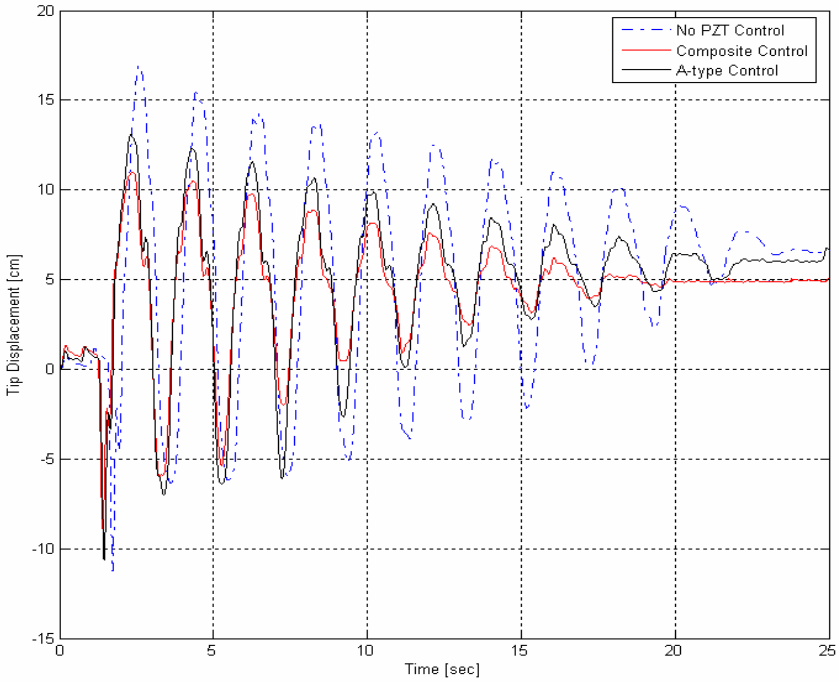

Figure 5.4. Comparison of closed-loop control responses with optimum gain selection

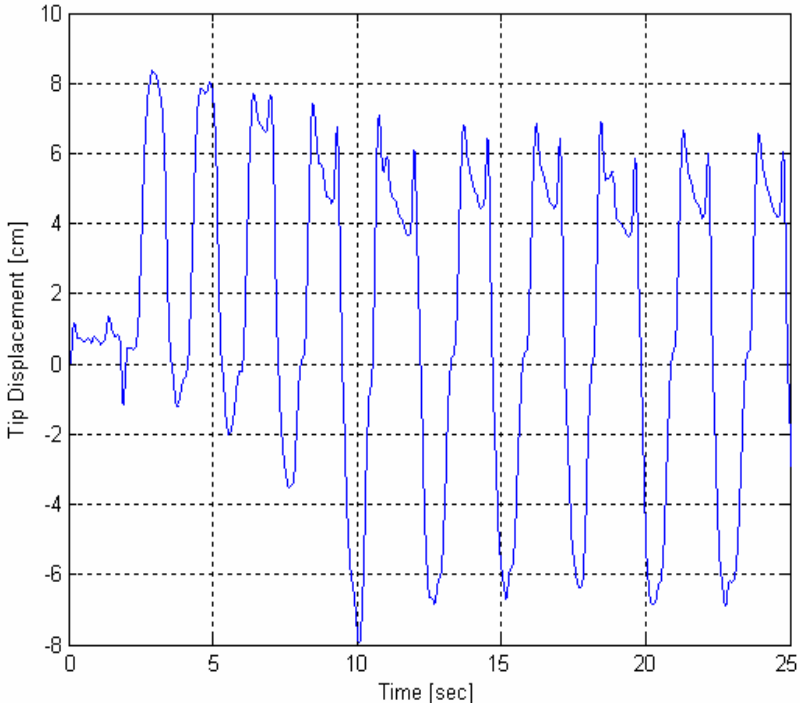

Figure 5.5. L-type controller response

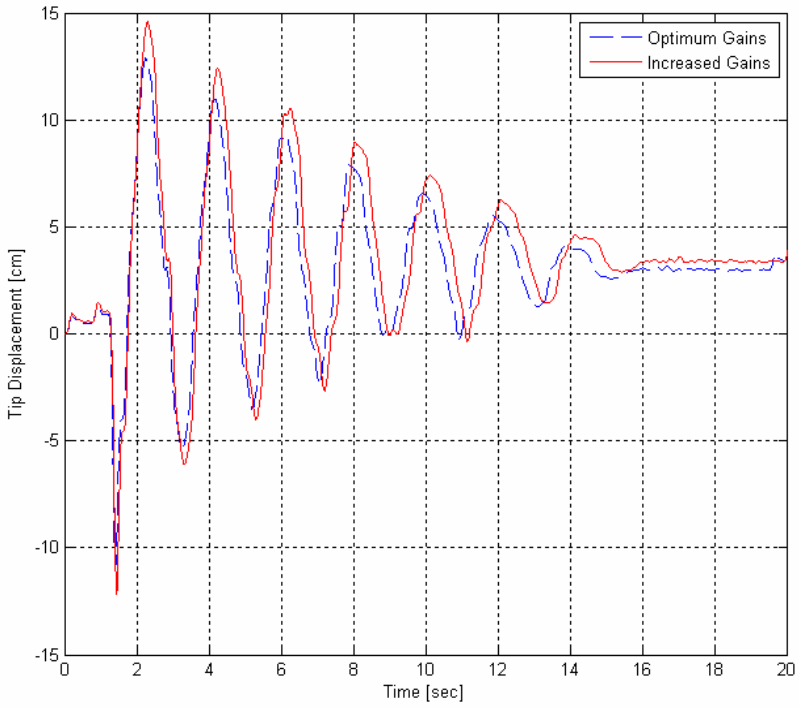

Figure 5.6. A-type controller response with different gains

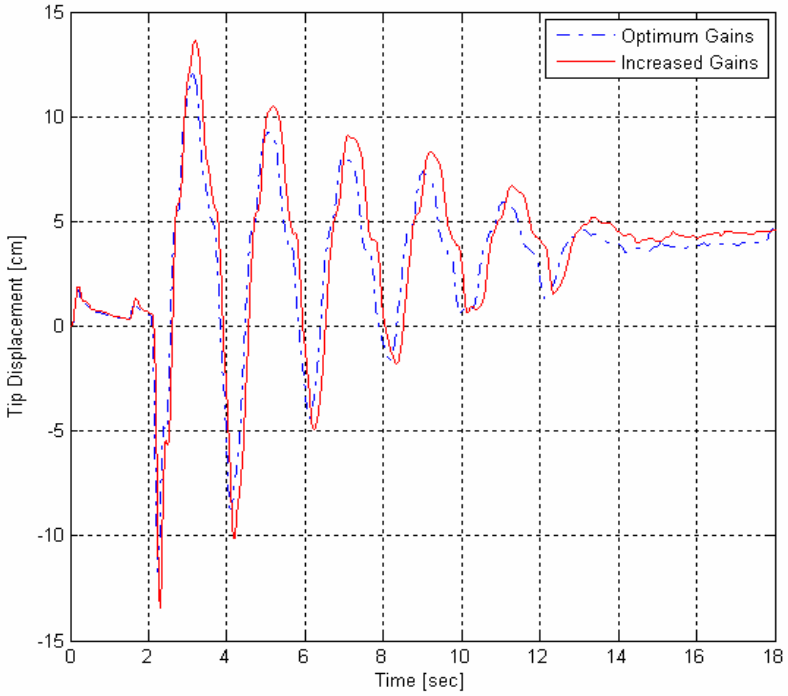

Figure 5.7. Composite controller response with different gains

Figure 5.8. Static shape deformation seen on the assembled beam (top view).

5.4 Verification of the ShapeTape™ Readings by Visualeyez™

The results shown above are based on the ShapeTape™ readings obtained during the experimental verification. In order to measure the reliability of the sensor array, another experiment was conducted: a sinusoidal input was provided to the hub and the subsequent response of the beam was acquired using ShapeTape™ and by an external sensor, Visualeyez™ (see Figure 5.9). The Visualeyez™ is a real-time, active-optical motion capture systems. It is typically used to perform motion capturing of the 3-D positions of infrared markers attached on a target object or human subject.

Figure 5.9. Visualeyez™ optical marker tracker system

The outputs of the sensors are shown in Figure 5.10. Considering the fact that there are measurement errors in ShapeTape™'s readings (as discussed in §5.3), the plots in Figure 5.10 shows that the general tip displacement profile of the flexible beam captured by the two sensing systems matches reasonably. The reason for the slight phase difference between the two systems is because of the half-duplex communication used by the ShapeTape™, and the difficulties in synchronizing the two systems.

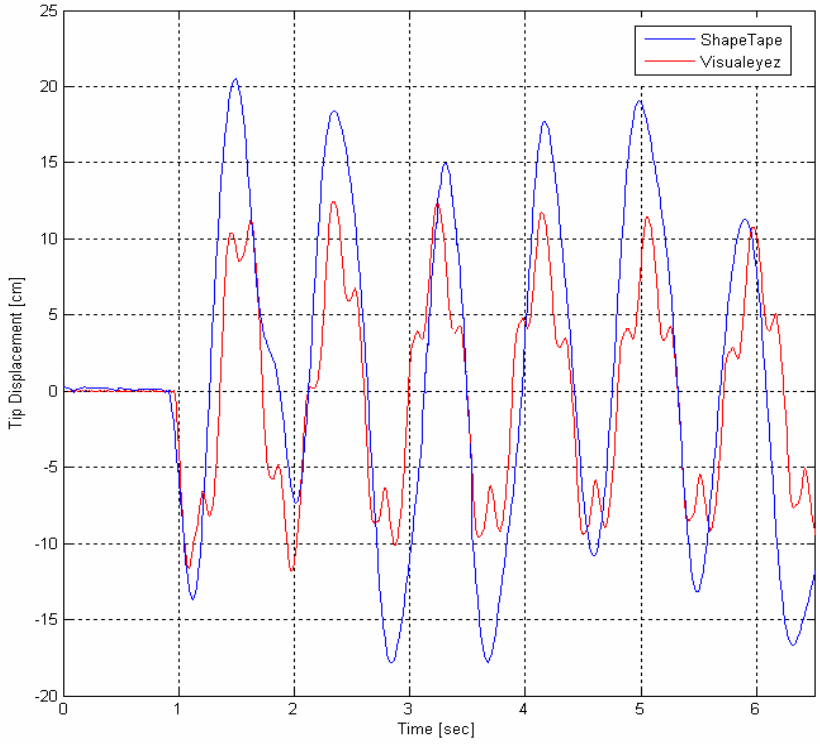

Figure 5.10. Visualeyez™ and ShapeTape™ optical sensor comparison

Chapter 6 CONCLUSIONS

Recent applications of lightweight flexible structures such as in slender robot arms, rotor blades, spacecrafts, and flexible hulled underwater vehicles has produced an increasing need for active structural control. In the heart of these studies, researchers have faced two major problems. One of the problems is the choice of a distributed actuating and sensing strategy. Piezoelectric actuators are synergistic with lightweight applications and are the predominant actuator technology: piezoelectrics themselves are lightweight and possesses excellent linearity over a wide frequency range. Secondly, in the development of a closed-loop control law for the distributed piezoelectric actuators, a suitable dynamics model must be selected – one that captures both the original system dynamics as well as any mechanical footprint left by the actuators and sensors themselves. Due to the underlying rigid-body motions generated by the primary actuators (e.g. the hub in the case of the single-link flexible manipulator) and the subsequent elastic motions of the flexible structure, modeling the flexible system dynamics can be challenging.

In Chapter 2 of this thesis, a discrete representation of an Euler-Bernoulli beam equipped with surface bonded piezoelectric actuators was derived. The dynamic modeling of the piezoelectric beam was completed following the Euler-Bernoulli approximation and Lagrange's equations. Using a total Lagrangian formulation, the governing differential equations of a finite segment of the flexible link were derived. The dynamic model included the inertial and damping effects of the surface bonded piezoelectric actuators as well as the centrifugal stiffening effect generated by hub motion. Assembling the finite element equations, a global system of equations was developed which were then used to derive L-typ and A-type PZT control laws using a Lyapunov criterion. Of these control laws, only the A-type approach was shown to assure stability of the flexible link. An existing L-type control was also presented, and it was proposed that the A-type and L-type controllers be combined into a new, composite control strategy. The A-type control was deemed possible because of a new shape sensing device called ShapeTape^{TM}, which can give both linear and angular velicity feedback.

In order to utilize the full potential of the three PZT controllers, a common problem in the vibration control field was addressed in Chapter 3 – the problem of properly choosing the actuator locations and feedback gains. In this chapter, the hub motion was removed from consideration in order to isolate the PZT effects. The transient response of the modeled piezoelectric flexible beam was cast into the form of a generalized eigenvalue problem, and it was found that the internal moments generated by the piezoelectric actuators created significant non-proportional damping in the system. Each of the three actuators used was placed separately by considering its effects on the first few modes of natural vibration when placed at several locations along the beam. The non-proportional

nature of the piezoelectric effects resulted in instabilities at some placements. In general, the A-type control yielded the most stable system behavior, compared to the L-type control. Also, it was found that an increase in the system's natural frequency of vibration, or chattering, could develop even for moderate gain values. The onset of chattering formed an upper bound on the gain values, which is something that has not been suggested in the existing literature.

The theoretical work in Chapter 3 suggested that the composite (L-type and A-type) controller should yield the best vibration suppression. This was validated using simulations and experiments that were summarized in Chapters 4 and 5, respectively. As explained in detail in Chapter 5, an experimental setup was built and it was shown that the proposed methods are applicable in real-time applications. It was observed that the presence of the angular velocity data in the control scheme not only ensures the stability, but also increases the controller performance in damping the vibration. For the experimental setup, all the gains and actuator placements were set based on the theoretical study of Chapter 3. The interfacing issues with the ShapeTape^{TM} , its inherent and systematic (due to our non-optimal installation method) measurement error and the limitation with the hub servomotor in the real-time setup all affected the experiments, and produce slight differences between experimental and simulation results. While the amplitude of the vibration followed the same pattern in both cases, it took a bit longer to suppress the vibration in real time. The main reason behind the longer suppression times in the experiments was the limited range of torques that could be produced by the hub's servomotor.

6.1 Contributions

The major contributions of this thesis are (i) the use of a novel fiber optic sensor array, called ShapeTape^{TM}, as an embedded feedback sensor for sensing angular deformations, as well as the linear deflections, of the manipulator; (ii) the design of a new piezoelectric controller, the composite L-type and A-type controller, for the use in the flexible link manipulator; (iii) a procedure, based on a fundamental generalized eigenvalue problem, for determining the optimal locations and gains for each individual PZT used, and; (iv) an experimental setup that can be used to verify proposed piezoelectric control methodologies.

6.2 Recommendations for Future Work

In the light of the results presented in this thesis, the experimental study for 2D vibration should be performed to use the advantages of the combined linear and angular velocity feedback in the vibration control on larger scale structures (e.g. aircraft wings) and nonlinear structures (e.g. very flexible structures). In addition to this, an improved design of fiber optic sensing technique is needed to measure both the linear and angular velocity data more accurately.

In order to immediately improve the current experiemental setup, the first action to take can be replacing the hub motor with another servomotor capable of generating higher torque. This action would enable us to observe more comparable results with the simulations. Second action can be addition of some model based filtration to the

ShapeTape™ signal conditioning to try and improve on the accuracy of the tip deflection measures.

APPENDIX A GENERALIZED EIGENVALUE PROBLEM

The technique used in actuator placement and gain selection procedure has led to a problem of the form:

$$\mathbf{\Psi t} = \mathbf{0} \tag{A.1}$$

where $\mathbf{\Psi}$ is an $m \times m$ matrix ($\mathbf{\Psi} = \mathbf{[M \quad C \quad K]}$ for the problem given in Eq. (3.1)) whose elements are polynomials in terms of x, and $\mathbf{t}$ is a nontrivial vector ($\mathbf{t} = \mathbf{[\ddot{x} \quad \dot{x} \quad x]}$ for the problem given in Eq.(3.1)), whose elements are of the form t^i where $i = 0,...,n$ with $n = m - 1$. A solution to this problem occurs when matrix $\mathbf{\Psi}$ is singular.

A matrix polynomial may be written as:

$$\mathbf{\Psi}(x) = \sum_{i=0}^{k} \Psi_i \lambda^i \tag{A.2}$$

where $\mathbf{\Psi}_i$ are $m \times m$ numerical matrices defined by the dynamics of the system as given in Eq. (3.1), λ is the variable of the matrix polynomial ($\lambda \equiv x$), and k is the largest degree of the variable λ in the polynomial matrix.

Assume that matrix $\mathbf{\Psi}_i$ is singular or close to being singular. If so, the inversion of $\mathbf{\Psi}_i$ can not be done, and the polynomial matrix can be written as a generalized eigenvalue problem. The roots of the determinant of the monic matrix polynomial $\mathbf{\Psi}(\lambda)$ are equivalent to the eigenvalues of the generalized system:

$$(\mathbf{K}_1\lambda - \mathbf{K}_2)\mathbf{T} = \mathbf{0} \tag{A.3}$$

where

$$\mathbf{K}_1 = \begin{bmatrix} \mathbf{I}_m & \mathbf{0}_m & \cdots & \mathbf{0}_m & \mathbf{0}_m \\ \mathbf{0}_m & \mathbf{I}_m & \cdots & \mathbf{0}_m & \mathbf{0}_m \\ \vdots & \vdots & \ddots & \mathbf{0}_m & \mathbf{0}_m \\ \mathbf{0}_m & \mathbf{0}_m & \cdots & \mathbf{I}_m & \mathbf{0}_m \\ \mathbf{0}_m & \mathbf{0}_m & \cdots & \mathbf{0}_m & \mathbf{\Psi}_k \end{bmatrix} \quad \text{and} \quad \mathbf{K}_2 = \begin{bmatrix} \mathbf{0}_m & \mathbf{I}_m & \mathbf{0}_m & \cdots & \mathbf{0}_m \\ \mathbf{0}_m & \mathbf{0}_m & \mathbf{I}_m & \cdots & \mathbf{0}_m \\ \vdots & \vdots & \ddots & \ddots & \vdots \\ \mathbf{0}_m & \mathbf{0}_m & \mathbf{0}_m & \cdots & \mathbf{I}_m \\ -\mathbf{\Psi}_0 & -\mathbf{\Psi}_1 & -\mathbf{\Psi}_2 & \cdots & -\mathbf{\Psi}_{k-1} \end{bmatrix} \tag{A.4}$$

with $\mathbf{0}_m$ and $\mathbf{I}_m$ being $m \times m$ null and identity matrices respectively.

Please refer to [24] for further details.

APPENDIX B SHAPE TAPE™

One of the key contributions of this work is the application of a novel sensor, ShapeTape™, into the flexible link as a feedback sensor. As illustrated in Figure B.1, the sensor is comprised of a serial array of fiber optic curvature sensors laminated on a long, thin ribbon substrate, or tape, geometrically arranged in such a way that the bend and twist of the ribbon's centerline can be measured. Each curvature sensor is an optical fiber formed into a tight loop, which is placed at approximately 45° to the ribbon's centerline axis [19]. Depending on bending or twisting that each curvature sensor experiences, the intensity of the light passing through the loop is varied. These fiber optic curvature sensors are linear, bipolar, and require minimal illumination [20].

As shown in Figure B.1.(Top), each pair of curvature sensors defines a sensing zone that produces bending and twisting values. These values can then be used to compute the path of the ribbon's centerline through the sensing zone. For example, the tangent to the ribbon's centerline, and a right handed Frenet frame that follows it, can be defined by:

$$\frac{\boldsymbol{d}\mathbf{r}}{\boldsymbol{ds}} = \hat{\mathbf{t}},\ \ \hat{\mathbf{n}} = \frac{1}{\kappa}\frac{\boldsymbol{d}\hat{\mathbf{t}}}{\boldsymbol{ds}} \ \text{ and } \ \hat{\mathbf{b}} = \hat{\mathbf{t}} \times \hat{\mathbf{n}} \tag{B.1}$$

respectively (see Figure B.2). Then, the Frenet-Serret equations define the changing orientation of the Frenet frame with respects to the arc length, *s*:

$$\frac{d\hat{\mathbf{t}}}{ds} = \kappa\hat{\mathbf{n}}\ ,\ \ \frac{d\hat{\mathbf{n}}}{ds} = -\kappa\hat{\mathbf{t}} + \tau\hat{\mathbf{b}} \ \text{ and } \ \frac{d\hat{\mathbf{b}}}{ds} = -\tau\hat{\mathbf{n}} \tag{B.2}$$

where $\hat{\mathbf{t}}$ is the tangential direction, $\hat{\mathbf{b}}$ is the binormal direction, $\hat{\mathbf{n}}$ is the normal direction, *s* is the arc length, κ is the curvature that arises due to bending, and τ is the geometric torsion of the ribbon's centerline that arises due to twisting. The bending occurs in the osculating plane which contains the normal and tangential directions.

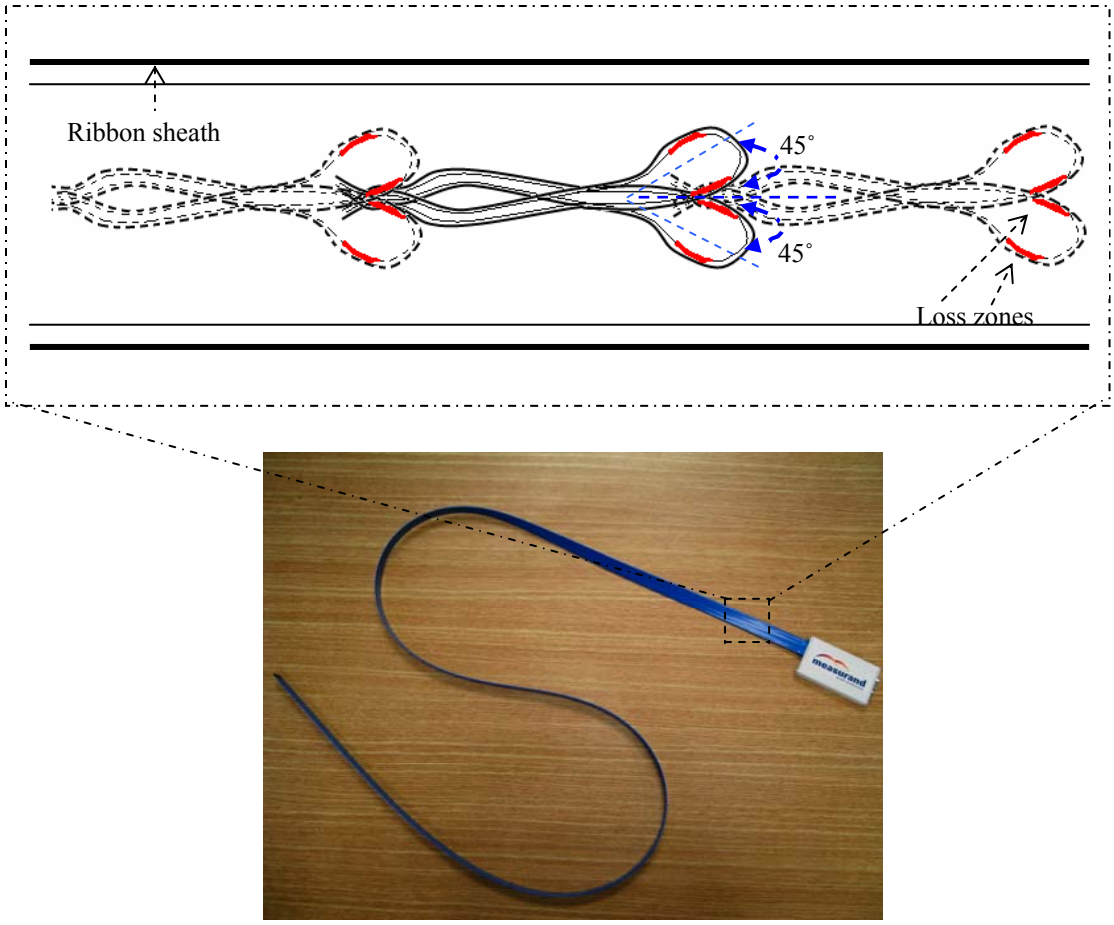

Figure B.1. (Top) Illustration of curvature sensors embedded in ShapeTape™. (Bottom) ShapeTape™ from Measurand.

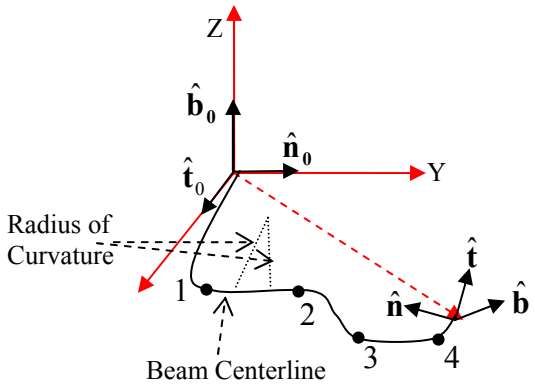

Figure B.2. Illustration of defined reference frames in ShapeTape™.

In the flexible link problem considered herein, the ribbon itself was completely embedded into the flexible beam, and their centerlines coincided, as shown in Figure 5.3 in §5. Note that because the beam has a preferred bending direction, and due to the fact that all externally applied loads pass through the shear centre of the beam's cross-section, no significant twist is expected during the planar slewing maneuvers. Thus, the twist can be assumed to be zero, which implies that the line of action of the binormal, $\hat{\mathbf{b}}$, is a constant.

Using the middle equation in Eq. (B.1), the change in the tangential direction, within the osculating plane, over a sensing zone can be found from:

$$\hat{\mathbf{t}}_i - \hat{\mathbf{t}}_{i-1} = \int \kappa \hat{\mathbf{n}} ds \tag{B.3}$$

where i represents the i^{th} point (or node) chosen along the ribbon, which is indicated with numbers in Figure B.2.

Given the zero twist condition, the normal vector, $\hat{\mathbf{n}}$, can be found using the middle equation of Eq. (B.2), i.e.

$$\hat{\mathbf{n}}_i - \hat{\mathbf{n}}_{i-1} = -\int \kappa \hat{\mathbf{t}} ds \tag{B.4}$$

Eqs (B.3) and (B.4) can be evaluated across a sensor domain independently using various integration techniques, and the Cartesian components of the updated tangent and normal vectors can be found. Then, the integral form of the first equation in Eq. (B.1) provides the displacement vector $\mathbf{r}(s)$ at the end of the sensing region.

$$\mathbf{r}_{\mathbf{i}+1} - \mathbf{r}_{\mathbf{i}} = \int \hat{\mathbf{t}} ds \tag{B.5}$$

Having specified $\hat{\mathbf{n}}$, $\hat{\mathbf{t}}$ and $\hat{\mathbf{b}}$ along the beam's centerline, pitch, yaw and roll angles can be found by using trigonometric relations [19], i.e.

$$\cos(\phi) = \sqrt{(b_Z n_Y / t_X}, \quad \cos(\theta^*) = \sqrt{b_Z t_X / n_Y}, \quad \cos(\psi) = \sqrt{n_Y t_X / b_Z} \tag{A.2.6}$$

The centerline displacement (**r**), the yaw (ψ), pitch (θ^*), and roll (ϕ) can be used to extract the state variables of the beam model. Since the beam is rotating about the global Z-axis, the nodal angles can be found simply by subtracting the hub angle from the yaw angle at the node location.

APPENDIX C MODELING OF PIEZOELECTRIC ACTUATORS

In this section, analytic model of the mechanical coupling of segmented PZT actuators to the dynamics of the structural member is developed. This leads to the capability to predict, a priori, the motion of the structural member in response to a specified excitation voltage across the PZT actuator. In order to establish the fundamental elastic coupling of the PZT/substructure system, a static model of actuators coupled to structures is developed for a surface-bonded actuator configuration. This coupling model is integrated into the finite element model introduced in Chapter 2 for the substructure. Furthermore, it is essential to understand the core of this modeling in order to have a complete understanding of the work presented. This model was introduced by Crawley et.al. [12] and it is incorporated in this work to define the virtual work done by the PZTs to have a complete description of the system equations and dynamic modeling.

For a surface-bonded actuator configuration, first static elastic model can be given ain the presence of a finite thickness elastic bonding layer between the substructure and PZT element, leading to a classic shear lag solution. When the shear lag in the bonding layer goes to zero, this solution can be reduced to a simpler model – that of a perfectly bonded PZT element.

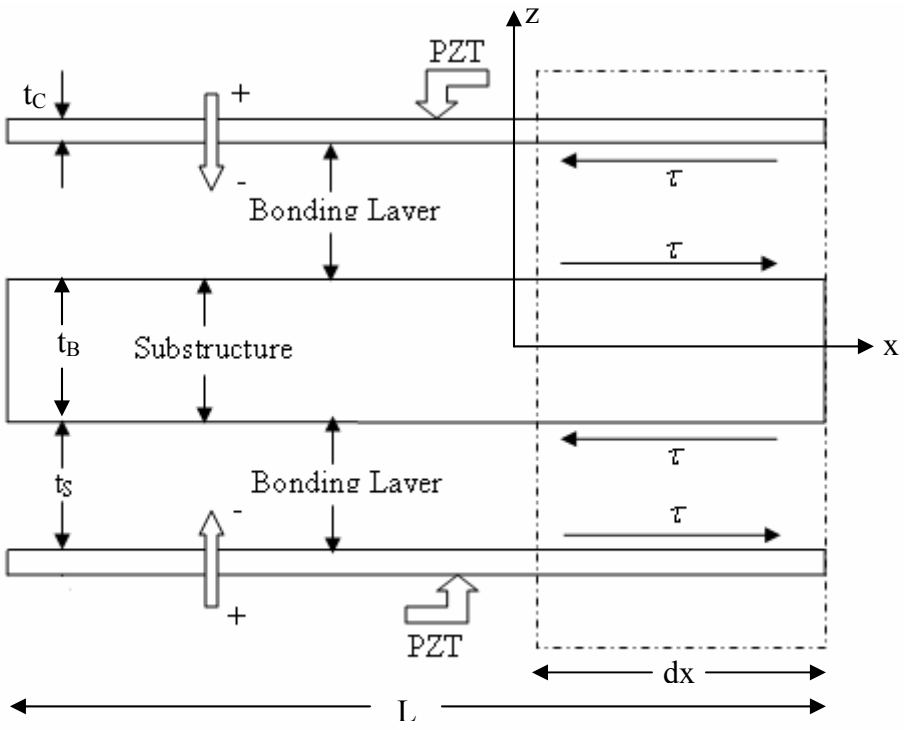

Figure C.1. Geometry of PZTs bonded to a flexible substructure

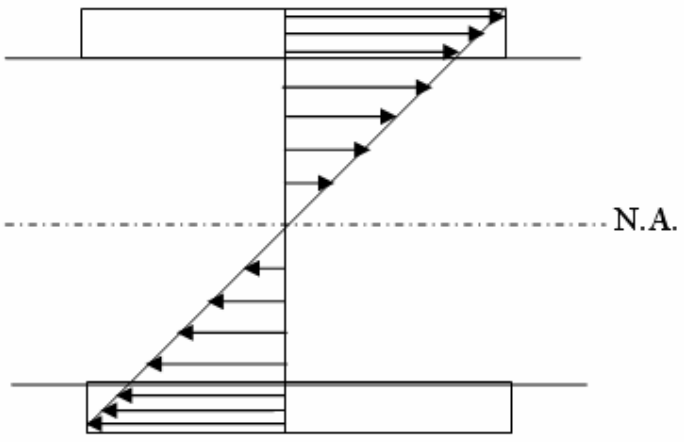

Figure C.2. Assumed PZT-substructure strain distribution

The dashed area in Figure C.1 is going to be investigated in order to get the equilibrium of the differential element. Pure one dimensional shear in the bonding layer and pure extensional strain in the PZT and substructure are considered. The strain and displacement relationships then can be given as

$$\varepsilon_C = \frac{\mathrm{d}u_C}{\mathrm{d}x} = u_C' \tag{C.1}$$

$$\varepsilon_B^s = \frac{\mathrm{d}u_B}{\mathrm{d}x} = u_B^{s\prime} \tag{C.2}$$

$$\gamma = \frac{u_C - u_B^s}{t_s} \tag{C.3}$$

Assuming Euler-Bernoulli strain distribution, the equilibrium equations for the dashed area in Figure C.1 become:

$$\frac{\mathrm{d}\sigma_C}{\mathrm{d}x} - \frac{\tau}{t_C} = 0 \tag{C.4}$$

$$\frac{\mathrm{d}\sigma_B^s}{\mathrm{d}x}+\frac{\alpha\tau}{t_B}=0 \tag{C.5}$$

where α is the constant varying based on the assumed beam strain, and it is 6 for Euler-Bernoulli strain distribution. The superscript *s* refers to the quantity on the surface of the beam.

The stress-strain relationship for the PZT element is similar to that of a thermoelastic material with the difference of PZT strain term $d_{31}V/t_C \equiv \Lambda$ in the form of [17]

$$\sigma_C = E_C(\varepsilon_C - \Lambda) \tag{C.6}$$

For the beam and the bonding layer, the stress-strain relations are:

$$\sigma_B^s = E_B\varepsilon_B^s \tag{C.7}$$

$$\tau = G\gamma \tag{C.8}$$

Substituting Eq. (C.3) into Eq. (C.8), inserting the Eqs. (C.4) and (C.5), and differentiating and substituting Eqs. (C.2), (C.6) and (C.7) results in two coupled second order differential equations:

$$\varepsilon_B^{s\ iv} - \Gamma^2\varepsilon_B^{s\prime\prime} = 0 \tag{C.9}$$

$$\varepsilon_C{}^{iv} - \Gamma^2\varepsilon_C{}'' = 0 \tag{C.10}$$

where differentiation is with respect to the nondimensional state $\bar{x}$. The shear lag parameter and the beam to the PZT stiffness ratio can be given as:

$$\Gamma^2 = \frac{G\theta_s}{t_s^2}\left(\frac{\psi+\alpha}{\psi}\right) \tag{C.11}$$

$$\psi = \frac{E_B t_B}{E_C t_C} \tag{C.12}$$

Solving Eqs. (C.9) and (C.10) for the strain distributions in the PZT and the substructure yields to:

$$\begin{bmatrix} \varepsilon_C \\ \varepsilon_B^s \end{bmatrix} = \begin{bmatrix} 1 \\ 1 \end{bmatrix} B_1 + \begin{bmatrix} 1 \\ 1 \end{bmatrix} B_2 \bar{x} + \begin{bmatrix} \frac{\psi}{\alpha} \\ 1 \end{bmatrix} B_3 \sinh \Gamma \bar{x} + \begin{bmatrix} -\frac{\psi}{\alpha} \\ 1 \end{bmatrix} B_4 \cosh \Gamma \bar{x} \tag{C.13}$$

As it can be seen in Eq. (C.13), the PZT strain term does not appear explicitly in the solution. However, two boundary conditions will let the PZT strain term appear. Under the assumption of that the regions underlying the ends of the actuator may have an arbitrary non-zero strain due to loading or deformation other than those caused by the action of the PZT, the boundary conditions are:

$$\bar{x} = +1: \qquad \varepsilon_C = \Lambda, \qquad \varepsilon_B^s = \varepsilon_B^{s+} \text{ and}$$

$$\bar{x} = -1: \qquad \varepsilon_C = \Lambda, \qquad \varepsilon_B^s = \varepsilon_B^{s-}$$

where ε_B^{s+} and ε_B^{s-} are the known substructure strain values at the right (+) and left (-) ends of the PZT.

By the help of the boundary conditions given above, Eq. (C.13) can be solved for the unknown constants, which are:

$$B_1 = \frac{\psi}{\psi + \alpha}\left(\frac{\varepsilon_B^{s+} + \varepsilon_B^{s-}}{2} + \frac{\alpha \Lambda}{\psi}\right) \tag{C.14.a}$$

$$B_2 = \frac{\psi}{\psi + \alpha}\left(\frac{\varepsilon_B^{s+} - \varepsilon_B^{s-}}{2}\right) \tag{C.14.b}$$

$$B_3 = \frac{\alpha}{(\psi + \alpha)\sinh\Gamma}\left(\frac{\varepsilon_B^{s+} - \varepsilon_B^{s-}}{2}\right) \tag{C.14.c}$$

$$B_4 = \frac{\alpha}{(\psi + \alpha)\cosh\Gamma}\left(\frac{\varepsilon_B^{s+} + \varepsilon_B^{s-}}{2} - \Lambda\right) \tag{C.14.d}$$

Substituting Eqs. (C.13) and (C.14) into Eqs. (C.1) and (C.2), integrating and substituting into Eq. (C.3) after inserting into Eq. (C.8) yields:

$$\frac{\tau}{E_B} = \frac{G}{t_s(E_B / E_C)\Gamma}\left[\frac{\varepsilon_B^{s+} - \varepsilon_B^{s-}}{2}\frac{\cosh\Gamma x}{\sinh\Gamma} + \left(\frac{\varepsilon_B^{s+} + \varepsilon_B^{s-}}{2} - \Lambda\right)\frac{\sinh\Gamma x}{\cosh\Gamma}\right] \tag{C.15}$$

The ability to strain or apply stress to the substructure actively, is represented by the terms dependent on Λ.

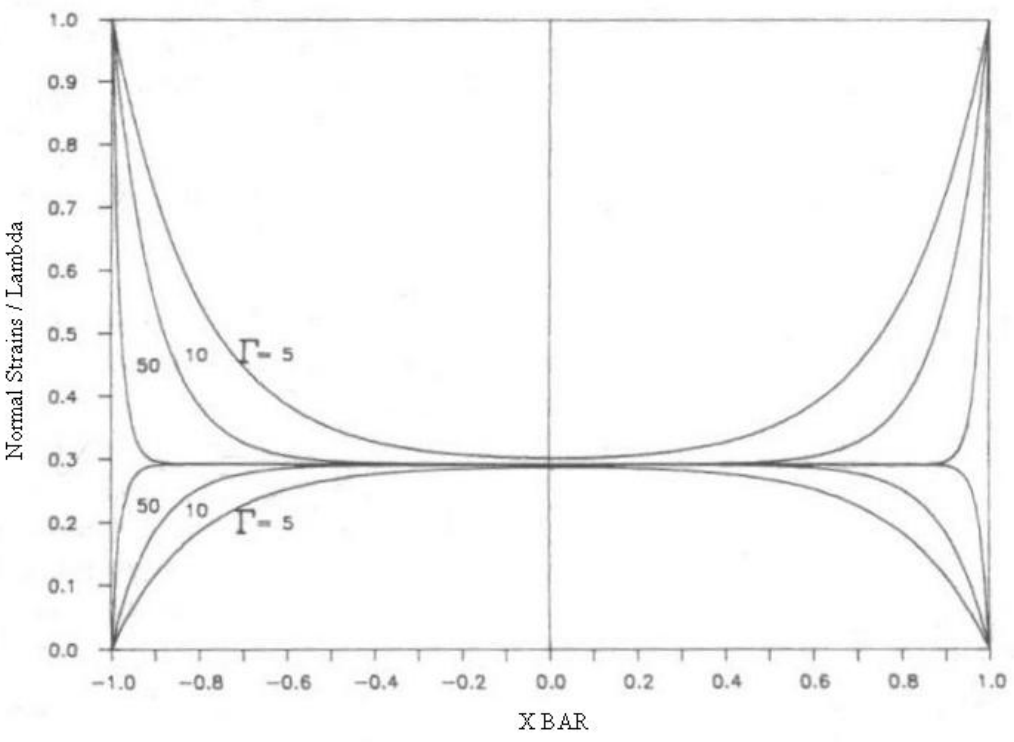

Figure C.3 Piezoelectric and substructure strain for various values, extracted from [12]

Solution for Perfectly Bonded Actuator

A perfectly bonded actuator represents the limiting case of an infinitely stiff bonding layer, with the shear lag parameter Γ approaching infinity. In this case, a sharp rise in the shear stress exists at the ends of the piezoelectric, indicating that the strain is transferred between the PZT and the substructure over an infinitesimal distance near the ends of the actuator, as seen in Figure C.1. The entire shear force is now effectively transferred at a concentrated point at the ends of the PZT. This force, applied at the ends of the PZT is:

$$\frac{F}{E_B t_b b} = \frac{1}{(\psi+\alpha)}\left[\frac{\varepsilon_B^{s+}+\varepsilon_B^{s-}}{2}+\left(\frac{\varepsilon_B^{s+}-\varepsilon_B^{s-}}{2}\right)\bar{x}\right]-\left[\frac{1}{(\psi+\alpha)}\right]\Lambda \qquad \text{(C.16)}$$

where the first part of the Eq. (C.16) represents the PZT stiffness and its effect on the substructure. However, the second part of the equation is the term regarding the force created by the ceramic due to the applied voltage and its material properties. One should keep in mind that, the stiffness effect of the PZT elements was taken into consideration during the finite element derivation and implemented with a lump model approach on top of the substructure considering the change in the cross section, inertia and the change Young's modulus of the element. Therefore, during the derivations of the Lagrangian equations, the forcing term was only created due to the generated bending moment in the presence of a control voltage, where the stiffness effect was already embedded into dynamics of the structure at relevant element.

BIBLIOGRAPHY

[1] Sun, D., Mills, J.K., Shan J., Tso S.K.: A PZT actuator control of a single-link flexible manipulator based on linear velocity feedback and actuator placement. Mechatronics **14**, 381-401 (2004)

[2] Homaifar, A., Shen, Y.: Vibration Control of Plate Structures Using PZT Actuators and Type II Fuzzy Logic. In: Proceedings of the American Control Conference, pp. 1575-1580. AACC, Arlington, USA (2001)

[3] Ghoshai, A., Wheater, E.A.: Vibration Suppresion Using a Laser Vibrometer and Piezoceramic Patches. Journal of Sound and Vibration **235(2)**, 261-280 (2000)

[4] Homaifar, A., Shen, Y.: Active Control of Flexible Structure Using Genetic Algorithms and LQG/LTR Approaches. In: Proceedings of the American Control Conference, pp. 4398-4402. AACC, San Diego, California (1999)

[5] Wang, X., Mills, J.K.: FEM dynamic model for active vibration control of flexible linkages and its application to a planar parallel manipulator. Applied Acoustics **66**, 1151–1161 (2005)

[6] Gopinathan, M., Pajunen, A.G.: Model reference control in vibrations in flexible smart structures. In: Proceedings of the 34th Conference on Decision & Control, pp. 3551- 3556. New Orleans, LA (1999)

[7] Homaifar, A., Shen, Y.: Vibration Control of Flexible Structures with PZT Sensors and Actuators. Journal of Vibration and Control **7(3)**, 417-451 (2001)

[8] Bathe, K.J., Bolourchi, S.: Large Displacement Analysis of Three-Dimensional Beam Structures. International Journal for Numerical Methods in Engineering **14**, 961-986 (1979)

[9] Chen, Z.Q., Agar, T.J.A.: Geometric Nonlinear Analysis of Flexible Spatial Beam Structures. Computers and Structures, **49(6)**, 1083-1094 (1994)

[10] Pai, P.F., Anderson, T.J., Wheater E.A.: Large-deformation Tests and Total-Lagrangian Finite Element Analyses of Flexible Beams. International Journal of Solids and Structures **37**, 2951-2980 (2000)

[11] Yigit, A., Scott, R.A., Ulsoy, A.G.: Flexural motion of a rotating beam attached to a rigid body. Journal of Sound and Vibration **121**, 201–210 (1988)

[12] Crawley, E.F., J. De Luis.: Use of piezoelectric actuators as elements of intelligent structures. AIAA Journal **25(10)**, 1373-1385 (1987)

[13] Zhang, X., Erdman, A.G.: Optimal Placement of Piezoelectric Sensors and Actuators for Controlled Flexible Linkage Mechanisms. Transactions of ASME **128**, 256-260 (2006)

[14] Fahroo, F., Wang, Y.: Optimal Location of Piezoceramic Actuators for Vibration Suppression of a Flexible Structure. In: Proceedings of the 36th Conference on Decision & Control, pp. 1966-1971. IEEE, San Diego, California (1997)

[15] Hiramoto, K., Doki, H., Obinata, G.: Optimal Sensor/Actuator Placement for Active Vibration Control Using Explicit Solution of Algebraic Riccati Equation. Journal of Sound and Vibration, **229(5)**, 1057-1075 (2000)

[16] Maxwell, N.D., Asokanthan, S.F.: Optimally Distributed Actuator Placement and Control for a Slewing Single-Link Flexible Manipulator. Smart Materials and Structures **12**, 287-296 (2003)

[17] Logan D.: A First Course in the Finite Element Method. PWS-KENT, Boston (1992)

[18] Setter N.: Pizeoelectric Materials in Devices. EPFL Ceramics Laboratory, Lausanne (1992)

[19] Danisch, L., Englehart, K.,Trivett A.: Spatially continuous six degree of freedom position and orientation sensor. Sensor Review, **19(2)**, 106-112 (1999)

[20] Danisch, L.A.: Fiber Optic Bending and Positioning Sensor with Selected Curved Light Emission Surfaces. US Patent 5,633,494, 27 May 1997

[21] Slotine J.J., Weiping Li: Applied Nonlinear Control. Prentice Hall, New Jersey (1991)

[22] Starek, L., Inman, D.J.: Design of Nonproportional Damped Systems via Symmetric Positive Inverse Problems. Transactions of ASME **126**, 212-219 (2004)

[23] Sorrentino, S., Marchesiello, S., Piombo, B.A.D.: A New Analytical Technique for Vibration Analysis of Non-Proportionally Damped Beams. Journal of Sound and Vibration **265**, 768-782 (2003)

[24] Watkins, S. David: Fundamentals of Matrix Computations. Wiley-Interscience, New York (2002)

[25] Queiroz, M.S., Dawson, D.M., Nagarkatti, S.P., Zhang, F.: Lyapunov Based Control of Mechanical Systems. Birkhauser, Boston (2000)

[26] Reddy, J.N.: An Introduction to the Finite Element Method, 3rd *Edition*. McGraw-Hill, New York (2006)

[27] Rao, S.S.: Mechanical Vibrations, 3rd *Edition*. Addison-Wesley, Massachusetts (1995)

[28] Junkins, J.L., Kim, Y.: Introduction to Dynamics and Control of Flexible Structures. AIAA Education Series, Washington, DC (1993)

[29] Meirovitch, L.: Methods of Analytical Dynamics. McGraw-Hill, New York (1970)

[30] Ginsberg, J.H.: Advanced Engineering Dynamics, *2nd Edition*. McGraw-Hill, New York (1970)

[31] Takeshi, M., Ryuichi, Y., Yasuhiro, O.: A Smooth Impact Rotation Motor Using a Multi-Layered Torsional PZT Actuator. IEEE Transactions on Ultrasonic, Ferroelectric and Frequency Control **46(6)**, 1439-1445 (1999)

[32] Pai, P.F., Nayfeh, A.H.: A Fully Nonlinear Theory of Curved and Twisted Composite Rotor Blades Accounting for Warpings and Three-Dimensional Stress Effects. International Journal of Solids and Structures **31(9)**, 1309-1340 (1994)

[33] Gilardi, G., Buckham, B.J., Park, E.: Finite Element Modeling of a Slewing Nonlinear Flexible Beam for Active Vibration Control with Arrays of Sensors and Actuators. Submitted to Computer & Structures (April 10, 2007).

UNIVERSITY OF VICTORIA PARTIAL COPYRIGHT LICENSE

Title of Thesis:

Dynamic Modeling and Vibration Control of a Single-Link Flexible Manipulator Using a Combined Linear and Angular Velocity Feedback Controller

Author: _____

Signed: _____